JACS
JOURNAL OF THE AMERICAN CHEMICAL SOCIETY

Article

Understanding and controlling short- and long-range electron/charge transfer processes in electron donor-acceptor conjugates

Ramandeep Kaur, Fabio Possanza, Francesca Limosani, Stefan Bauroth, Robertino Zanoni, Timothy Clark, Giorgio Arrigoni, Pietro Tagliatesta, and Dirk M. Guldi

J. Am. Chem. Soc., **Just Accepted Manuscript** • DOI: 10.1021/jacs.0c01452 • Publication Date (Web): 14 Mar 2020

Just Accepted

is published by the American Chemical Society. 1155 Sixteenth Street N.W., Washington, DC 20036

Understanding and controlling short- and long-range electron/charge transfer processes in electron donor-acceptor conjugates

Ramandeep Kaur[a‡], Fabio Possanza[b‡], Francesca Limosani[b‡], Stefan Bauroth[c‡], Robertino Zanoni[d], Timothy Clark[c], Giorgio Arrigoni[e,f], Pietro Tagliatesta[b]*, Dirk M. Guldi[a]*

[a]Interdisciplinary Center for Molecular Materials, Department of Chemistry and Pharmacy, Friedrich-Alexander-University Erlangen-Nuremberg, Egerlandstrasse 3, 91058 Erlangen, Germany
[b]Department of Chemical Science and Technologies, University of Rome Tor Vergata, Via della Ricerca Scientifica 1, 00133 Rome, Italy
[c]Computer-Chemistry-Center and Interdisciplinary Center for Molecular Materials, Department of Chemistry and Pharmacy, Friedrich-Alexander-University Erlangen-Nuremberg, Nägelsbachstrasse 25, 91052 Erlangen, Germany
[d]Department of Chemistry, University of Rome "La Sapienza", Piazzale Aldo Moro 5, 00185 Rome, Italy
[e]Department of Biomedical Sciences, University of Padova, Via U. Bassi 58/B, Padova, Italy
[f]Proteomics Center, University of Padova and Azienda Ospedaliera di Padova, via G. Orus 2/B, Padova, Italy

ABSTRACT: We have probed a series of multicomponent electron donor$_2$-donor$_1$-acceptor$_1$ conjugates, both experimentally and computationally. The conjugates are based on the light harvester and primary electron-donor zinc-porphyrin (ZnP, donor$_1$), to whose *β*-positions a secondary electron-donor ferrocene (Fc, donor$_2$) and the primary electron-acceptor C_{60}-fullerene (C_{60}, acceptor$_1$). Novel is linking all of them *via p*-phenylene-acetylene/acetylene bridges of different lengths to gain full control over shuttling electrons and holes between C_{60}, ZnP, and Fc Different charge-separation, charge-transfer, and charge-recombination routes have been demonstrated, both by transient absorption spectroscopy measurements on the femto, pico-, nano-, and microsecond time scales and by multi-wavelength and target analyses. The molecular wire-like nature of the *p*-phenylene-acetylene bridges as a function of C_{60}-ZnP and ZnP-Fc distances is decisive in the context of generating distant and long-lived **$C_{60}^{\bullet-}$-ZnP-Fc$^{\bullet+}$** charge-separated states. *For the first time*, we confirm the presence of two adjacent charge-transfer states, a **C_{60}-ZnP$^{\bullet-}$-Fc$^{\bullet+}$** intermediate in addition to **$C_{60}^{\bullet-}$-ZnP$^{\bullet+}$-Fc,** *en route* to the distant **$C_{60}^{\bullet-}$-ZnP-Fc$^{\bullet+}$** charge-separated state. Our studies demonstrate how the interplay of changes in the reorganization energy and the damping factor of the molecular bridges, in addition to variation in the solvent polarity, affect the outcome of charge-transfer and the corresponding rate constants. The different regions of the Marcus parabola are highly relevant are highly relevant in this matter: The charge-recombination of, for example, the adjacent **$C_{60}^{\bullet-}$-ZnP$^{\bullet+}$-Fc** charge-separated state is located in the inverted region, while that of the distant **$C_{60}^{\bullet-}$-ZnP-Fc$^{\bullet+}$** charge-separated state lies in the normal region. Here, the larger reorganization energy of Fc relative to ZnP makes the difference.

INTRODUCTION

The natural photosynthetic reaction centers have served as blueprints for solar light harvesting technology, and thus provided a major driving force for studying and characterizing a myriad of artificial electron donor-acceptor systems.[1-3] The distinct light harvesting and electron-donation properties of (metallo)porphyrins render them perfect building blocks for electron donor-acceptor conjugates. Electron-accepting fullerenes provide the perfect counterpart to (metallo)porphyrin electron donors.

Important groundwork has already been laid with respect to both the reorganization energy of C_{60} in electron-transfer reactions and the damping factor of π-conjugated molecular bridges.[4-8] The small reorganization energy of fullerenes in electron transfer reactions means that, in combination with (metallo)porphyrins such as that of zinc (ZnP) in C_{60}-ZnP electron donor-acceptor conjugates, charge-separation and charge-recombination are found in the normal and the inverted region of the Marcus parabola, respectively. This is independent of the electron donor-acceptor distance.[9-14] A different picture evolves, however, for the corresponding ferrocene C_{60}-Fc electron donor-acceptor conjugates, in which charge-separation and charge-recombination are both found in the normal region of the Marcus parabola. The only notable exception of a Marcus inverted behavior for the charge-recombination is caused by very short electron donor-acceptor distances between C_{60} and Fc.[9, 15-17]

An important physico-chemical parameter that assists in regulating the interplay between electron-donor and -acceptor is the damping factor of the molecular bridge. Ideally, molecular bridges with small damping factors enable electronic coupling and, in turn, electron transfer over large distances.[18-22] Thus, recent attention has been focused on π-conjugated oligo-phenylene-vinylenes[23-26], polyacetylenes[10], oligo-phenylenes[27-29], oligo-phenylene-ethynylenes[30-36], and oligo-

thiophenes[37, 38]. Importantly, they feature damping factors from as small as 0.03 Å^{-1} to as large as 0.2 Å^{-1} for oligo-phenylene-vinylenes and oligo-phenylenes, respectively. Such a broad range of values is key in modulating the rates of short- and long-range electron transfer by orders of magnitude.

We have now investigated how the interplay of changes in the reorganization energy and the damping factor affect short- and long-range electron transfer dynamics in a series of multicomponent electron donor-acceptor conjugates. C_{60} is common to all conjugates and serves as the electron-acceptor. Notable differences in their oxidation potentials and reorganization energies were incentives to use ZnP and Fc as primary and secondary electron-donors, respectively. The most important feature of the electron donor-acceptor conjugates is the linkage of the secondary electron-donor Fc and the electron-acceptor C_{60} to the primary electron-donor ZnP: *β*-positioning activates the unprecedented pathway of forming the C_{60}-ZnP$^{\bullet-}$-Fc$^{\bullet+}$ intermediate *en-route* to the $C_{60}^{\bullet-}$-ZnP-Fc$^{\bullet+}$ charge-separated state. Overall, the resulting electron donor-acceptor separations in the corresponding C_{60}-ZnP-Fc span the range from 12 to 40 Å. In addition, *p*-phenylene-acetylenes/acetylene were employed as bridges to tune the shuttling electrons and holes between C_{60}, ZnP, and Fc, which, to the best of our knowledge, has never be done before.

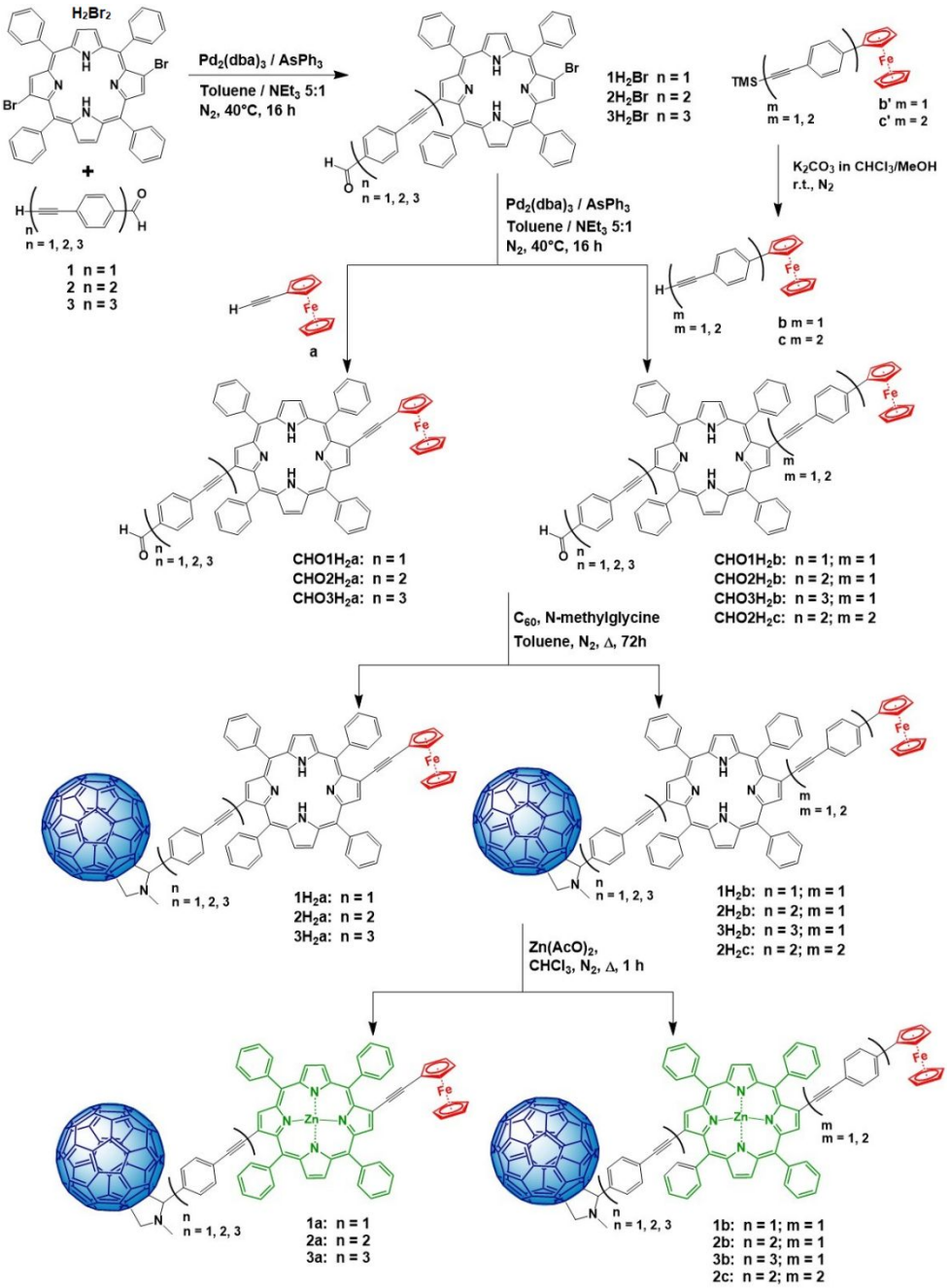

Figure 1. *Synthetic routes towards C_{60}-ZnP-Fc electron donor-acceptor conjugates.*

RESULTS AND DISCUSSION

Design and Synthesis

Lately, we have reported on the *β*-functionalization of H_2TPP by one or two ferrocenes in the 2- and 3-positions through either ethynyl or phenylethynyl functionalities.[39] At the time, it was employed as a novel use of the Sonogashira reaction to enable investigations of the intramolecular energy and/or electron transfer following light excitation.[37]

In the following years, we set our focus on the synthesis of *β*-modified porphyrins that feature electron-accepting C_{60}. For example, a series of different molecular bridges were used to connect the porphyrins and the fullerenes and to study the impact of substituents on the intramolecular transduction of energy and/or electrons.[32, 40] Soon after that, several reports from other groups with the focus on the synthesis and characterization of different tetraphenylporphyrins bearing electron donating ferrocenes at the *β*-, meso-, or 4-phenyl positions followed.[11, 12, 14-17, 22, 26] We, on the other hand, have functionalized the 2,12 positions of H_2TPP with fullerenes and ferrocenes as electron-acceptors and -donors, respectively. By employing either ethynyls or ethynylphenylenes, we realized new hybrid materials with push-pull character[32-34], using, for example, new carbon material (Carbon Spheres-CSs) as acceptor unit.[41] The possibility to place different substituents at the *β*-pyrrole positions constitutes a powerful approach towards the fine-tuning of tetrapyrroles, in general, and the modulation of electron donor-acceptor interactions, in particular.

In this paper, we synthetized two new molecular electron-donor acceptor systems. They are based on the extension of the conjugation via *β*-substitution resulting in push-pull effects. They are a combination of electron-donors (i.e., ferrocene), light-harvester (i.e., porphyrin) and electron-acceptors (i.e., C_{60}) connected to each other through "molecular wires" of variable lengths. On one hand, a meso-tetraphenylporphyrin was connected to a ferrocene in its *β*-position through oligo *p*-phenyleneethynylenes using the Sonogashira reaction. On the other hand, C_{60} was linked to the *β*-position of the *meso*-tetraphenylporphyrin using the Prato–Maggini reaction.[42] Importantly, the different molecular bridges have been directly linked to the *β*-pyrrolic positions to create, in turn, a set of a novel electron donor-acceptor system.

Figure 1 summarizes the synthetic pathways for obtaining the different multicomponent electron donor-acceptor conjugates. The first step involved a Sonogashira coupling of **H_2Br_2** with 1.5 equivalents of the different *p*-phenyleneethynylenes (**1-3**) and afforded porphyrins **1-3H_2Br**.[32-34] The stereochemistry of 2,12-dibromo TPP as starting material was recently elucidated.[43] The next step was again a Sonogashira coupling reaction between **1-3H_2Br** and two equivalents of different ferrocenes (**a-c**) to afford the corresponding intermediates **CHO1-3H_2(a-c)**. For the functionalization of C_{60} with intermediates **CHO1-3H_2(a-c)**, we used the Prato-Maggini reaction[32-34] *en route* to **1-3H_2(a-c)**. In the final step, zinc was inserted following a literature procedure to yield **1-3(a-c)** quantitatively.

The photophysical properties of the **1-3(a-c)** conjugates were then investigated by comparing them at different stages with the relevant references.[44] The references used include the commercially available **ZnTPP**, **C_{60}-ref.**, ***β*-ZnP-ref**. (Mass and NMR spectra, and the structureof ***β*-ZnP-ref**. available in Figures S25-26), and already published ZnP-Fc conjugates[39] **HZnPa, HZnPb** (Figure S27).

Absorption Spectroscopy

In order to provide insight into the ground-state characteristics of the conjugates, the absorption spectra of **1a** and **1b** are compared in Figure 2. The spectra feature in the UV region absorptions of C_{60} and the characteristic Soret- and Q-band absorptions of ZnP in the visible region with extinction coefficients as high as 1.4 x 10^5 and 1.5 x 10^4 M^{-1} cm^{-1}, respectively. In addition, the acetylene-phenylene/phenylene-acetylene bridges absorb in the 330 to 350 nm range.[32] Due to the relatively low extinction coefficient of Fc, that is, approximately 90 M^{-1} cm^{-1} no direct absorption is observed.[9]

At first glance, a comparison with the **ZnTPP** references (Figure SP1) reveals broadened and red-shifted Soret-band absorptions in **HZnPa**, **HZnPb**, **1-3a, 1-3b**, **and 2c** (Figures SP2-3, SP5-8). Relative to the ZnP-Fc conjugates all conjugates baring C_{60} as electron-acceptor, that is, **1-3a, 1-3b** and **2c,** exhibit even more broadened and red-shifted absorption bands (Figure SP4). All of the changes stem from the substitution at the *β*-pyrrole- rather than *meso*-positions and, in turn, perturb the ZnP ground state. The lower symmetry of the porphyrin also contributes to the broadening and red shifts. These changes get stronger with the integration of the phenylene-acetylene bridges between C_{60} and ZnP or the phenylene/ acetylene-phenylene bridges between ZnP and Fc.

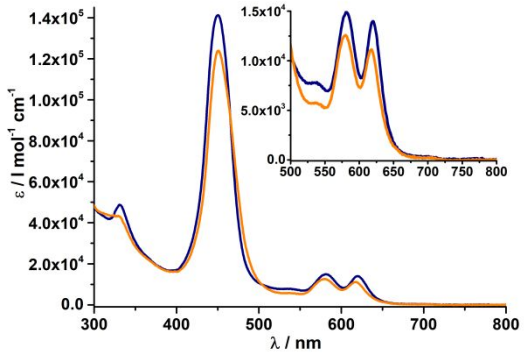

***Figure 2**. Absorption spectra of **1a** (navy blue) and **1b** (orange) in chlorobenzene under ambient conditions; inset shows the Q-band absorption.*

A closer inspection of the Q(0,0) to Q(1,0) ratio sheds light onto the energetic differences between the two degenerate ^{1}E (a_{2u}, e_g) and E (a_{1u}, e_g) levels. Ratios of around 0.50 in **HZnPa** and **HZnPb** and 0.9 in **1-3a, 1-3b and 2c** are considerably larger than that of 0.19 found for the **ZnTPP** reference. These values indicate a perpetual effect on the degeneracy of the energy levels with consecutive *β*-pyrrole substitution. The reason behind this is a non-zero electron density of the a_{1u} orbital at the *β*-position relative to the a_{2u} orbitals. It perturbs the two π a_{1u} and a_{2u} orbitals differently and, in turn, leads to a larger energy difference in the conjugates than in **ZnTPP**.[45]

Fluorescence Spectroscopy

The only meaningful fluorescent probe in the series of C_{60}-ZnP-Fc conjugates **1-3a, 1-3b,** and **2c** is that of ZnP. For example, fluorescence spectra of the **ZnTPP** reference feature maxima at 595 and 645 nm and a quantum yield of 0.33 in toluene (Figure SP9). C_{60} fluoresces, but its low quantum yield of 10^{-4} hampers accurate analyses, especially in the presence of the electron-donating ZnP and Fc. In the corresponding conjugates, we note red shifts and significant quenching of the ZnP fluorescence relative to **ZnTPP**; the quantum yields are in the range of 6.7×10^{-5} to 1.9×10^{-2}. A closer look at the quantum yields reveals that they increase as a function of the C_{60}-ZnP distance, the non-polar character of the solvent, and the ZnP-Fc distance. First, placing one, two, or three phenylene-acetylene units between C_{60} and ZnP with distances of 12.6, 19.5, and 26.4 Å, respectively, leads to quantum yields of 1.3×10^{-4}, 2.0×10^{-3}, and 6.4×10^{-3} in benzonitrile, respectively. Second, in toluene the corresponding quantum yields are 5.6×10^{-4}, 9.4×10^{-3}, and 1.9×10^{-2}. Third, an increase in the ZnP-Fc distance from 12.6 Å to 19.5 Å by increasing the number of acetylene-phenylene units from one to two changes the quantum yields from 2.0×10^{-3} to 3.5×10^{-3} (Figures SP11-16).

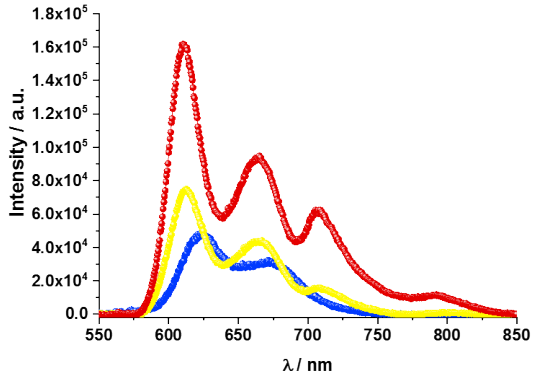

***Figure 3**. Fluorescence spectra of **1b** measured in solvents of different polarity, that is, toluene (red), chlorobenzene (yellow), and benzonitrile (blue), with an excitation wavelength of 435 nm.*

At this point, the thermodynamic driving forces for charge-separation and the underlying solvent dependence suggest that the ZnP fluorescence quenching is due to a charge transfer evolving between the ZnP singlet excited state and C_{60}·-, which involves ZnP as the electron donor. A reasonable charge-transfer alternative is the charge-transfer pathway between the ZnP singlet excited state and Fc, which implies that ZnP acts as an electron acceptor. This notion is not only supported thermodynamically, but also the 90% ZnP fluorescence quenching observed in the **HZnPa** and **HZnPb** implies excited state interactions between ZnP and Fc (Figure SP9-10). Energy transfer, for example, from the ZnP singlet excited state to C_{60} cannot be ruled out, especially in the non-polar solvent toluene, where the C_{60} fluorescence at 708 and 790 nm is noticed. In non-polar solvents, the excitation spectra of the C_{60} fluorescence are in sound agreement with the ZnP absorption spectra (shown for **1b** in Figure SP17). As the solvent polarity is, however, increased, the energy-transfer pathway is deactivated (Figure 3).

X-ray Photoelectron Spectroscopy

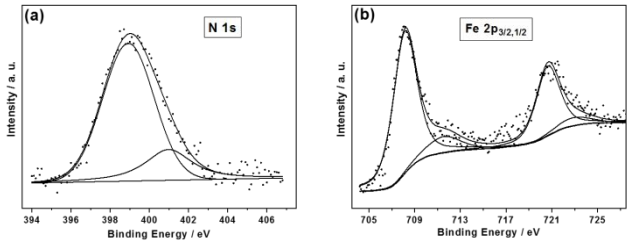

***Figure 4. (a)** N 1s (left) and Fe 2p **(b)** photoemission spectra of **1b**. Experimental data points and theoretically reconstructed spectra are presented by dots and solid lines, respectively.*

XPS analyses of **1a** and **1b** enable not only corroborating the presence of Fe, Zn, and N, but also their relative atomic ratios by means of probing the presence and intensity of their 2*p*, 2*p*, and 1*s* peaks, respectively. A leading example is presented in Figure 4 for the N *1s* and Fe *2p* spectra of **1b**. A 1.0:1.2:5.0 atomic ratio between Fe, Zn, and N is derived for **1b**. The atomic ratio of 4:1 for the N 1*s* peaks at 398.9 and 401.0 eV confirms the presence of the (metallo)porphyrin and the fullerene. Importantly, the presence of Fe(II) and Fe(III) in a 4:1 ratio, derived from the two $2p_{3/2}$ peaks at 708.1 and 711.5 eV (weak intensity) suggests a partial electron-transfer with ferrocene.

Electrochemistry

The redox potentials of **C_{60}-ref.**, **Fc-ref.** (for structures see Figure S28) and ***β*-ZnP-ref.** which were used as references, and the corresponding C_{60}-ZnP-Fc conjugates were determined next to the absorption and fluorescence characteristics. This is done to rationalize the electron-transfer events, both between ZnP and C_{60} and between ZnP and Fc. The thermodynamic driving forces for any electron-transfer processes in the electron-donor-acceptor conjugates were based on the differential pulse voltammograms. These were recorded in dichloromethane by using tetrabutylammoniumhexafluorophosphate (NBu_4PF_6) as supporting electrolyte - Table 1.[46] In the case of C_{60} its first and second reductions occur at −1.09 and −1.41 V, respectively. When turning to ***β*-ZnP-ref**, in addition to the first reduction at −1.55V, the first and second oxidations are noted at +0.43 and +0.74 V, respectively. For Fc, only a single oxidation is seen at +0.39 V. (Figure S18) For **1a** of the **1-3a** series, the first reduction at −0.95 V and the second reduction at −1.33 V are C_{60}-centered, while the first oxidation at +0.15 V and the second oxidation at +0.49 V take place on Fc and ZnP, respectively (Figure SP19).

***Table 1.** Redox potentials (corrected against Fc/Fc^+ internal standard) of the references and conjugates **1a** and **1b** recorded in argon-saturated dichloromethane with NBu_4PF_6 as supporting electrolyte, Ag/Ag^+ as reference electrode, Pt as counter electrode, and glassy carbon as working electrode at a scan rate of 0.01 V s^{-1}.*

	C_{60} Reduction		ZnP reduction	Fc Oxidation	ZnP Oxidation	
β-ZnP-ref.	-	-	–1.55	-	+0.43	+0.74
C_{60}-ref.	–1.41	–1.09	-	-	-	-
1a	–1.33	–0.95	–1.42	+0.15	+0.49	+0.83
1b	–1.42	–1.03	–1.50	+0.05	+0.42	+0.86

Similarly, for **1b** of the **1-3b** series, two reductions at –1.03 and –1.42 V are centered on C_{60}, while oxidations at +0.05 and +0.42 V involve Fc and ZnP, respectively.

In both series and for **2c** the number of *p*-phenylene-acetylenes between the electron-accepting C_{60} and the electron-donating ZnP/Fc has no appreciable impact on neither the reductions nor the oxidations (Table SP1) (Figure SP20). From this finding, we conclude the absence of appreciable electronic couplings in the ground state; a postulate which is independently confirmed by the electrochemical behavior of the references.

Thermodynamic Driving Forces

From the redox potentials in dichloromethane, the thermodynamic driving forces for the charge-separation (Equation 1), charge- recombination (Equation 2), and even charge-shift were determined in different solvents using the Rehm-Weller equation.[47] The approach takes the Gibbs free energy of the charge-separated state in solvents of different dielectric constants ε_s into account. Here, *e* is the elementary charge, $E_{OX}(D/D^{\bullet+})$ and $E_{RED}(A/A^{\bullet-})$ are the first oxidation of the electron-donor and the first reduction of the electron-acceptor in dichloromethane (ε_{ref} = 8.93), respectively. E_{00} is the energy of the ZnP first singlet excited state (2.04 eV) and ΔG_{SOL} is the solvent correction term, which accounts for Coulombic interactions in the charge-separated state in solvents of different polarity.[47,48]

$$\Delta G^{\circ}_{CR} = [e(E^{ox}(D/D^{\bullet+}) - E^{red}(A/A^{\bullet-}))] - \Delta G_{SOL} \quad (1)$$

$$\Delta G^{\circ}_{CS} = [e(E^{ox}(D/D^{\bullet+}) - E^{red}(A/A^{\bullet-})) - E_{00}(ZnP)] - \Delta G_{SOL} \quad (2)$$

$$\Delta G_{SOL} = \frac{e^2}{4\pi\varepsilon_0\varepsilon_s R_{DA}}\frac{1}{} + \frac{e^2}{4\pi\varepsilon_0}\left[\left(\frac{1}{2r_{D^+}} + \frac{1}{2r_{A^-}}\right)\left(\frac{1}{\varepsilon_{ref}} - \frac{1}{\varepsilon_s}\right)\right] \quad (3)$$

In equation 3, ε_0 is the permittivity of the vacuum, R_{DA} is the electron donor-acceptor distance, and r_{D+} and r_{A-} are the ionic radii of the electron-donor and -acceptor, respectively. From Table 2 we conclude that all thermodynamic driving forces are sufficiently exergonic. In turn, all charge-separation, charge-recombination, and charge-shift reactions should occur. Increasing the solvent polarity from toluene to benzonitrile decreases the energies and results in even further increased driving forces. For example, the energies of the charge-separated states in benzonitrile are 1.37 and 1.03 eV for $C_{60}^{\bullet-}$-$ZnP^{\bullet+}$-Fc and $C_{60}^{\bullet-}$-ZnP-$Fc^{\bullet+}$, respectively, and 1.52 eV for C_{60}-$ZnP^{\bullet-}$-$Fc^{\bullet+}$. For the pathway *via* the $C_{60}^{\bullet-}$-$ZnP^{\bullet+}$-Fc intermediate, the values in benzonitrile are -0.67, -0.34, and -1.37 eV, respectively. For the pathway involving the C_{60}-$ZnP^{\bullet-}$-$Fc^{\bullet+}$ intermediate, charge-separation, charge-shift, and charge-recombination are exothermic in benzonitrile by -0.52, -0.49, and -1.52 eV, respectively.

Table 2. *Thermodynamic driving forces (–ΔG° in eV) for the charge-separation (CS), charge-recombination (CR), and charge-shift (CSh) reactions in solvents of different polarities determined for* ***1b*** *using the Rehm-Weller equation*

Initial State	Final State	$-\Delta G^{\circ}_{CS/CR/CSh}$ / eV			
		toluene (ε_s = 2.28)	chlorobenzene (ε_s = 5.62)	benzonitrile (ε_s = 25.2)	dimethylformamide (ε_s = 36.7)
C_{60}–^{1*}ZnP–Fc	**C_{60}–$ZnP^{\bullet-}$–$Fc^{\bullet+}$**	0.22	0.41	0.52	0.52
C_{60}–^{1*}ZnP–Fc	**$C_{60}^{\bullet-}$–$ZnP^{\bullet+}$–Fc**	0.37	0.56	0.67	0.68
C_{60}–$ZnP^{\bullet-}$–$Fc^{\bullet+}$	**$C_{60}^{\bullet-}$–ZnP–$Fc^{\bullet+}$**	0.37	0.47	0.49	0.49
$C_{60}^{\bullet-}$–$ZnP^{\bullet+}$–Fc	**$C_{60}^{\bullet-}$–ZnP–$Fc^{\bullet+}$**	0.22	0.32	0.34	0.35
C_{60}–$ZnP^{\bullet-}$–$Fc^{\bullet+}$	**C_{60}–ZnP–Fc**	1.82	1.63	1.52	1.52
$C_{60}^{\bullet-}$–$ZnP^{\bullet+}$–Fc	**C_{60}–ZnP–Fc**	1.67	1.48	1.37	1.36
$C_{60}^{\bullet-}$–ZnP–$Fc^{\bullet+}$	**C_{60}–ZnP–Fc**	1.41	1.12	0.99	0.98

.

Molecular Modeling

The series of C_{60}-ZnP-Fc conjugates and the individual building blocks, C_{60}, ZnP, and Fc, were investigated with density functional theory (DFT) at the B3LYP and Cam-B3LYP//cc-pVDZ level of theory using the Gaussian16 program.[49–52] Geometries were optimized using the PCM solvation model with benzonitrile as solvent.[53–59] For all conjugates, linear arrangements proved to be the thermodynamically most stable configuration. Interestingly, all bridges, which link C_{60} and Fc with ZnP are planar, although the α-substituted phenylenes cause steric hindrance and result in an 8° offset from linearity in the C-C-C angle. **1a** shows two

rotational barriers, which are placed along the rotation of the cyclopentadienyl planes relative to the ZnP-plane. They are found to be 4.2 and 0.6 kcal·mol^{-1} at the orthogonal positions of Fc with respect to the ZnP plane (Figure ST1). Bridge elongation, like in **1b**, leads to reduced steric hindrance and 0.6 kcal mol^{-1} for both transition structures. The ZnP to Fc distances (Table ST1) are 8.3, 12.6 and 19.5 Å in **1a**, **2a**, and **3a**, respectively, while the C_{60} to ZnP distances are 12.6, 19.5 and 26.4 Å in **1a**, **1b**, and **1c**, respectively.

To understand the effect of *β*-pyrrole substitution on ZnP, the corresponding molecular orbitals were plotted and analyzed (see Figure ST2-6). Energetically, the highest occupied molecular orbital (HOMO) is hardly affected and shows a less than 10 meV change with respect to the ZnTPP reference. This is interesting, as the former a_{2u} orbital is changed significantly and gives rise to a significant bridge-centered contribution. In contrast, the former a_{1u} orbital remains localized on ZnP, despite a stabilization of up to 95 meV. A similar picture evolves for the degenerated lowest unoccupied molecular orbitals (LUMOs), e_{gx} and e_{gy}. For e_{gx}, a rather large contribution is found on the bridge, which assists in stabilizing it. The e_{gy} is local and only weakly stabilized. Overall, the HOMO-LUMO gap is lowered by 0.3 eV relative to that in the ZnP reference. Notably, the impact of different bridge lengths is minor. A conclusion that is consistent with the electrochemical and spectroscopic results.

Next, time-dependent DFT (TD-DFT) single-point calculations were carried out to obtain the vertical excitation energies (Figure ST8, Table ST2). In all cases, two low lying singlet-excited states S_1 and S_2 are present. The energy of S_1 ranges from 2.14 – 2.15 eV, independent of the ZnP-C_{60} distance, but dependent on the distance between Fc and ZnP. Equally weak is the stabilization of S_2, which depends, however, on both distances. For both singlet-excited states, a dipole moment is found that is larger than that in the ground state. Moreover, it depends on the ZnP-Fc distance (Table ST3). These observations suggest charge-transfer character for S_1 and S_2. The changes in electrostatic potential between ground and the first six singlet-excited states are shown in Figure ST9. In S_1 and S_2, the electron density is increased on ZnP and decreased on Fc, resulting in a $ZnP^{\delta-}$–$Fc^{\delta+}$ charge-transfer state. S_3 and S_4 are mainly ZnP-centered and feature a strong coupling into the bridges. Compared to a ZnP reference, the degeneracy is cancelled and the molecular orbital energies are stabilized by up to 0.15 eV. This is consistent with the spectroscopic studies. Analyses of the natural transition orbitals (B3LYP, Figure ST10-T13) proof the strong interplay of all three building blocks, yielding multiple excited states with charge transfer character.

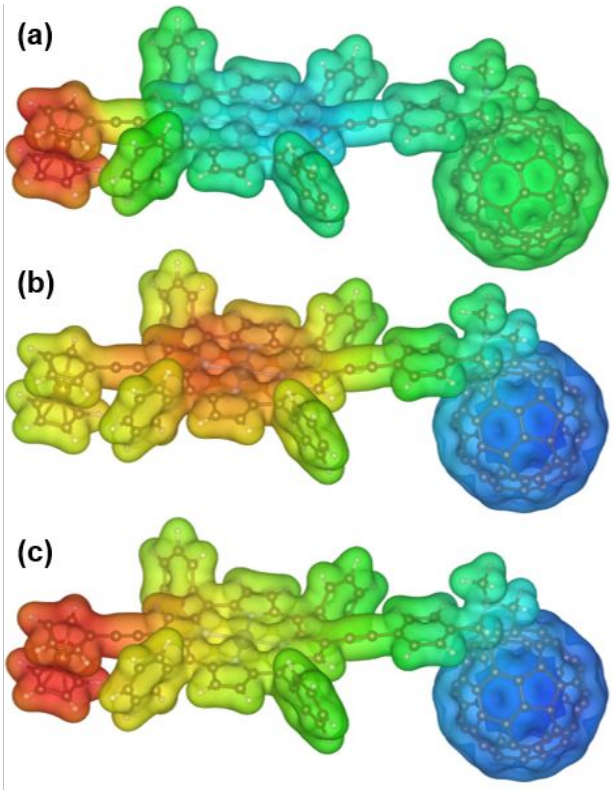

Figure 5. *Electrostatic potential difference between excited and ground state for **1a**, mapped on the ground state electron density isosurface (isovalue = 0.015): **(a)** fully optimized charge transfer state C_{60}–$ZnP^{\bullet-}$–$Fc^{\bullet+}$ (E=1.63 eV, dipole moment 5.3 D, blue= -0.025, red= 0.025), **(b)** partially optimized charge separated states $C_{60}^{\bullet-}$–$ZnP^{\bullet+}$–Fc (E=1.59 eV, dipole moment 78.1 D, middle, -0.1 – 0.1) and **(c)** $C_{60}^{\bullet-}$–ZnP–$Fc^{\bullet+}$ (E_V =1.50 eV, dipole moment 88.2 D, bottom, -0.1 – 0.1).*

Finally, the excited states were optimized for **1a** and **2c** to estimate the driving forces for the excited-state deactivation. Particular focus was placed on the first CT-excited state (Figure 5a). Reduction of ZnP in conjugates of C_{60}, ZnP, and Fc is rather unusual and the main deactivation involves the $C_{60}^{\bullet-}$-$ZnP^{\bullet+}$-Fc intermediate prior to any charge-shift *en route* to the $C_{60}^{\bullet-}$-ZnP-$Fc^{\bullet+}$ charge-separated state. Importantly, the driving force, which was determined for the S_1 deactivation in, for example, **1a** is –0.53 eV; in excellent agreement with the electrochemically based value of –0.51 eV. In other words, we expect a competition between the formation of the $C_{60}^{\bullet-}$-$ZnP^{\bullet+}$-Fc and C_{60}-$ZnP^{\bullet-}$-$Fc^{\bullet+}$ intermediates in the overall ZnP deactivation. The full charge-separated states (Figure 5b and c) were not directly accessible from excited-state calculations at the ground state geometry. To access them we partially optimized the excited state based on the preoptimized anion geometry. The high dipole moment of 78 and 88 Debye for b and c confirm the fully charge-separated state character of these states. Although overestimated due the partial optimization procedure, the derived energies of 1.59 and 1.50 eV for $C_{60}^{\bullet-}$-$ZnP^{\bullet+}$-Fc and the $C_{60}^{\bullet-}$-ZnP-$Fc^{\bullet+}$, respectively, are in line with the proposed redox cascade.

Transient Absorption Measurements

To shed light onto the photoexcited state deactivation, the characterization of the photoproducts, and the determination of the rate constants, we turned to pump-probe experiments in the femto-, pico-, nano-, and microsecond regimes. In particular, transient absorption spectra were recorded after exciting ZnP in the electron donor-acceptor conjugates **1a-3a**, **1b-3b** and **2c** at 568 nm. The ZnP singlet-excited state features evolve immediately after excitation and include maxima at 480-490, 600, and 650 nm, together with ground state bleaching of the Soret- and Q-band absorptions at 450 and 620 nm. Unlike ***β*-ZnP-ref**. (Figures SP23-24), these singlet excited-state features transform into a new transient species within 2 to 10 ps. This species is characterized by fingerprints in the visible range, around 415 and 650 nm, and in the near-infrared at 1010 nm; they relate to the one-electron oxidized form of ZnP (Figure SP21) and to the one-electron reduced form of C_{60}, respectively. We, therefore, conclude that the ZnP singlet-excited state transforms into the $C_{60}^{\bullet-}$-$ZnP^{\bullet+}$-Fc charge-separated state. Importantly, multi-wavelength analysis of the decay of the $C_{60}^{\bullet-}$-$ZnP^{\bullet+}$-Fc charge-separated state shows that it is monophasic for the one-electron oxidized form of ZnP and biphasic for the one-electron reduced form of C_{60} (see Figure 6a,b). In addition, the short lifetime of the former matches that of the latter. We postulate the involvement of Fc in a charge-shift reaction and, in turn, the generation of the $C_{60}^{\bullet-}$-ZnP-$Fc^{\bullet+}$ charge-separated state. Unambiguous proof for the presence of the one-electron oxidized form of Fc is made difficult by its low extinction coefficient of 90 M^{-1} cm^{-1}. However, the calculations support our conclusions – vide supra.

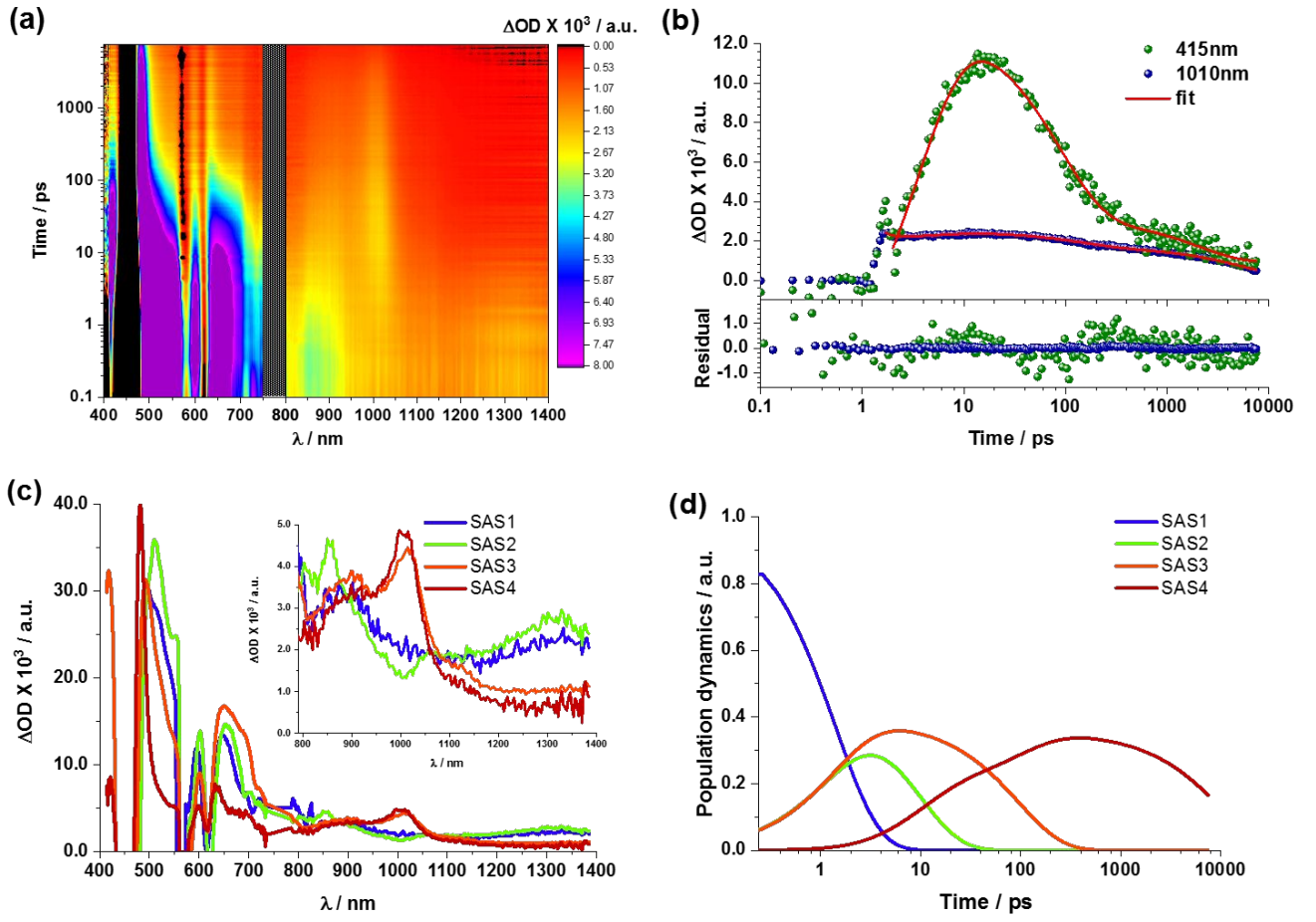

Figure 6 (a). *Femtosecond-transient absorption spectroscopy fs-TAS of* ***1b*** *recorded with several time delays between 0.5 and 7500 ps in the visible and near-infrared region (λ_{exc} = 568 nm) in argon-saturated benzonitrile at room temperature.* ***(b).*** *Time absorption profiles of $ZnP^{\bullet+}$ at 415 nm (green), and $C_{60}^{\bullet-}$ at 1010 nm (navy blue), obtained in fs-TAS (λ_{exc} = 568 nm) in argon-saturated benzonitrile illustrating the decay of the excited states with the corresponding fits and the residual of the fits.* ***(c).*** *Deconvoluted transient absorption species associated spectra of* ***1b*** *in argon-saturated benzonitrile with C_{60}–^{1*}ZnP–Fc (SAS1 – blue), C_{60}–$ZnP^{\bullet-}$–$Fc^{\bullet+}$ (SAS2 – green), $C_{60}^{\bullet-}$–$ZnP^{\bullet+}$–Fc (SAS4 – red), $C_{60}^{\bullet-}$–ZnP–$Fc^{\bullet+}$ (SAS5 – brown) obtained via target analysis in GloTaran.* ***(d).*** *Population dynamics of SAS1, SAS2, SAS3, and SAS4.*

In addition to multi-wavelength analysis, we subjected the transient absorption data to global target analysis, which is based on an excited-state deactivation kinetic model and involves the R-package TIMP and the graphical user interface GloTarAn.[60] The energies for the excited states and the one-electron oxidized and reduced of the respective component constitute the basis for the kinetic model - (Figure 7) - and involve four species in benzonitrile. Figure 6c, d shows the species associated spectra and the associated population dynamics for **1b** obtained upon global-target analysis.

The deconvoluted species relate well to the kinetic model. For example, the first species is the ZnP singlet-excited state, which is formed instantaneously upon photoexcitation featuring maxima at 495, 593 and 644 nm and minima at 611 nm. It transforms in a parallel fashion into the second and the third species, which are the C_{60}-$ZnP^{\bullet-}$-$Fc^{\bullet+}$ and $C_{60}^{\bullet-}$-$ZnP^{\bullet+}$-Fc charge-separated states, respectively, *via* two competitive charge-separation steps with rate constants k_{CS1} and k_{CS2}. The two charge-separated states both exhibit the fingerprint absorptions due to the one-electron oxidized and the one-electron reduced forms of the respective components.

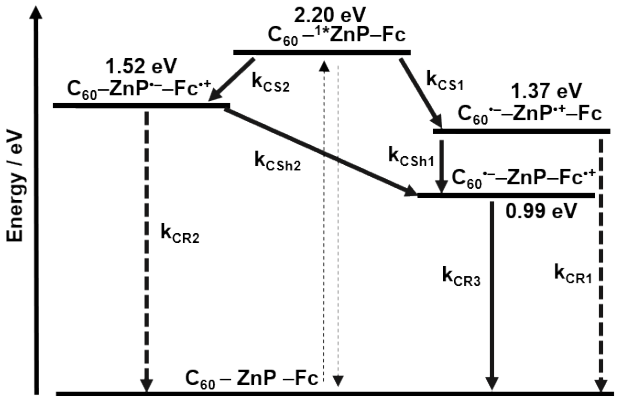

***Figure** 7: The kinetic model applied to deconvolute excited state species of the conjugates in benzonitrile via target analysis in GloTaran.*

SAS2, which is referred to as the C_{60}-$ZnP^{\bullet-}$-$Fc^{\bullet+}$ charge-separated state, features the same spectral characteristics, which is gathered for the ZnP-Fc conjugate **HZnPb**. It exhibits a distinct shoulder at 550 nm and the excited state absorption features are broadened in comparison to the spectroelctrochemically generated one-electron reduced form of ZnP (Figure SP29). For **1-3a,** SAS2, next to its similarity with the differential absorption of the corresponding ZnP-Fc conjugate **HZnPa**, agrees well with the differential absorption spectra of the spectroelctrochemically one-electron reduced form of ZnP (Figure SP33). Features, which are observed for SAS3, comprise the one-electron oxidized form of the ZnP transients at 415 nm and broad maxima spanning from 630 to 700 nm in the visible region (Figures SP30, SP34). In the near-infrared region, the characteristic 1010 nm fingerprint of the one-electron reduced form of C_{60}, implies the formation of the $C_{60}^{\bullet-}$-$ZnP^{\bullet+}$-Fc charge-separated state.[4,8,14-17]

The fate of both charge-separated states involves either the ground state recovery *via* charge-recombination with rate constants k_{CR1} and k_{CR2} or the population of the fourth state, the $C_{60}^{\bullet-}$-ZnP-$Fc^{\bullet+}$ charge-separated state *via* charge-shift with rate constants k_{CSH1} and k_{CSH2}.[61] Finally, the $C_{60}^{\bullet-}$-ZnP-$Fc^{\bullet+}$ charge-separated state converts into the ground state *via* charge recombination with the rate constant k_{CR3}.

In the **1-3a** series, the conjugate., which features the shortest electron donor-acceptor separations, both between C_{60} and ZnP and between ZnP and Fc, the parallel formation of the $C_{60}^{\bullet-}$-$ZnP^{\bullet+}$-Fc and C_{60}-$ZnP^{\bullet-}$-$Fc^{\bullet+}$ charge-separated state takes place with rate constants k_{CS1} and k_{CS2} of 2.80×10^{11} and 3.11×10^{11} s^{-1}, respectively. For the subsequent charge-shift reactions to populate accordingly the $C_{60}^{\bullet-}$-ZnP-$Fc^{\bullet+}$ charge-separated state we determined k_{CSH1} and k_{CSH2} to be 7.50×10^{9} and 7.40×10^{10} s^{-1}, respectively, before the ground state is recovered with k_{CR3} = 6.21×10^{8} s^{-1} (Figures SP31-32). In the **1-3b** series and **2c**, the larger ZnP-Fc separation in **1b** slows down k_{CS2} to 2.30×10^{11} s^{-1}, k_{CSH2} to 3.90×10^{10} s^{-1}, and k_{CR3} to 1.01×10^{8} s^{-1}. Relative to either **1a** or **1b**, increasing the C_{60} to ZnP distance in **2a** and **3a**, on one hand, or **2b**, **3b**, and **2c**, on the other, leads to subtle changes in the kinetic model. Rather than seeing the parallel formation of the C_{60}-$ZnP^{\bullet-}$-$Fc^{\bullet+}$ and $C_{60}^{\bullet-}$-$ZnP^{\bullet+}$-Fc charge-separated state, the latter is mediated by the population of a vibrationally relaxed ZnP singlet-excited state - Figure SP22. Evidence is given by small blue shifts of the ground state bleaching of the Soret-band absorption. In **2a** and **3a,** only the k_{CS1}s are different but not the k_{CS2}s: 1.07×10^{10} s^{-1} for **2a** and 9.60×10^{8} s^{-1} for **3a**. In **2b** and **3b**, the k_{CS1}s are 9.10×10^{9} and 1.25×10^{9} s^{-1}, respectively. In light of the aforementioned, charge-shift k_{CSH1}, that is, the $C_{60}^{\bullet-}$-$ZnP^{\bullet+}$-Fc to $C_{60}^{\bullet-}$-ZnP-$Fc^{\bullet+}$ charge-separated state transformation is rather inefficient in **2a**, **3a**, **2b**, and **3b**; instead the $C_{60}^{\bullet-}$-ZnP-$Fc^{\bullet+}$ charge-separated state is mainly populated in these cases *via* charge-shift at rates k_{CSH2} comparable to those in **1a** and **1b**. Also, in the conjugates **2a**, **3a**, **2b**, and **3b**, due to a slower k_{CS1}, a significant contribution of the ^{3*}ZnP is seen at longer time delays. Notably, k_{CR3} decreases from 6.21×10^{8} s^{-1} in **1a**, to 1.23×10^{8} s^{-1} in **2a**, and to 7.70×10^{5} s^{-1} in **3a** and from 1.01×10^{8} s^{-1} in **1b** to2.58×10^{6} s^{-1} in **2b** and to 4.76×10^{5} s^{-1} in **3b**. (see Figures SP35-42)

To overcome the bottleneck of the charge-separation k_{CS1} and charge-shift k_{CSH1} cascade, but without compromising the overall C_{60}-Fc distance, we took, for example, **2c** and decreased the C_{60} to ZnP distance, on the one hand, and increased the ZnP to Fc distance, on the other. In **2c**, k_{CS1}, with 9.50×10^{9} s^{-1} is indeed competitive with k_{CS2} and, in turn, is followed by a k_{CSH1} of 7.50×10^{8} s^{-1} (Figures SP43-44). It is not surprising that the $C_{60}^{\bullet-}$-ZnP-$Fc^{\bullet+}$ charge-separated state is formed in **2c** with higher quantum yields than in **3b**. The slow-down of the charge recombination leading to k_{CR3}s as low as 2.90×10^{5} s^{-1} is quite remarkable.

A strong solvent polarity dependence was found forconjugates **1-3a, 1-3b**, and **2c**, especially on going from non-polar to moderately or highly polar solvents. The impact on both the formation and decay kinetics of the charge-separated states and the overall mechanism of deactivation is particularly strong. In toluene, the energies of the $C_{60}^{\bullet-}$-$ZnP^{\bullet+}$-Fc, C_{60}-$ZnP^{\bullet-}$-$Fc^{\bullet+}$, and $C_{60}^{\bullet-}$-ZnP-$Fc^{\bullet+}$ charge-separated states with values of 1.67, 1.82, and 1.45 eV favor a charge recombination into the triplet-excited states of either ZnP (1.53 eV) or C_{60} (1.50 eV)[9] (Figures SP45-51). As a result, the ZnP or C_{60} triplet-excited states dominate the product of charge-recombination, before the recovery of the ground state sets in. In both moderately polar

chlorobenzene and highly polar benzonitrile and dimethylformamide, the energies of stabilized charge-separated states fall below those of either the ZnP or C_{60} triplet-excited states. In turn, the ground state recovery is direct rather than indirect. (Figures SP52-70)

Table 3. *Rate constants for the different charge transfer processes in conjugates 1-3b in benzonitrile as obtained via target analysis in GloTaran.*

Initial State	Final State		k / s^{-1}			
		Type	**1b**	**2b**	**3b**	**2c**
			n = 1, m = 1	n = 2, m = 1	n = 3, m = 1	n = 2, m = 2
C_{60}–^{1*}ZnP–Fc	**$C_{60}^{\bullet-}$–ZnP$^{\bullet+}$–Fc**	k_{CS1}	2.60×10^{11}	9.10×10^{9}	1.25×10^{9}	9.50×10^{9}
C_{60}–^{1*}ZnP–Fc	**C_{60}–ZnP$^{\bullet-}$–Fc$^{\bullet+}$**	k_{CS2}	2.30×10^{11}	2.0×10^{11}	2.1×10^{11}	-
$C_{60}^{\bullet-}$–ZnP$^{\bullet+}$–Fc	**$C_{60}^{\bullet-}$–ZnP–Fc$^{\bullet+}$**	k_{CSh1}	1.80×10^{9}	-	-	7.50×10^{8}
C_{60}–ZnP$^{\bullet-}$–Fc$^{\bullet+}$	**$C_{60}^{\bullet-}$–ZnP–Fc$^{\bullet+}$**	k_{CSh2}	3.90×10^{10}	2.20×10^{10}	1.20×10^{10}	-
$C_{60}^{\bullet-}$–ZnP$^{\bullet+}$–Fc	**C_{60}–ZnP–Fc**	k_{CR1}	2.80×10^{9}	1.40×10^{9}	2.56×10^{8}	1.10×10^{9}
C_{60}–ZnP$^{\bullet-}$–Fc$^{\bullet+}$	**C_{60}–ZnP–Fc**	k_{CR2}	4.80×10^{10}	4.30×10^{10}	2.25×10^{10}	-
$C_{60}^{\bullet-}$–ZnP–Fc$^{\bullet+}$	**C_{60}–ZnP–Fc**	k_{CR3}	1.01×10^{8}	2.58×10^{6}	4.76×10^{5}	2.90×10^{5}

Reorganization Energies, Damping Factors, and Electronic Couplings

In short, we have determined the electron-transfer mechanism in a series of C_{60}-ZnP-Fc conjugates with the help of multi-wavelength, global, and target analyses and have determined the underlying rate constants, starting with the photoexcitation of ZnP all the way to the complete ground state recovery. The lifetimes of the $C_{60}^{\bullet-}$-ZnP$^{\bullet+}$-Fc and $C_{60}^{\bullet-}$-ZnP-Fc$^{\bullet+}$ charge-separated states exhibit strong, but different correlations with the solvent polarity. For example, with increasing solvent polarity, the lifetimes of the $C_{60}^{\bullet-}$-ZnP$^{\bullet+}$-Fc charge-separated states decrease. In stark contrast, the lifetimes of the $C_{60}^{\bullet-}$-ZnP-Fc$^{\bullet+}$ charge-separated states increase with increasing solvent polarity -Table 4. Based on equation 4 as part of the Marcus theory,[8,9] we gather a sound understanding of solvent polarity effects by means of analyzing the plots of the driving forces *vs*. rate constants charge recombination. In equation 4, '*V*' is the electronic coupling matrix element, k_B the Boltzmann constant, *h* the Planck constant, *T* the absolute temperature, and 'λ' the reorganization energy. Notably, we did not use equation 4 to obtain '*V*' and '*λ*' due to the fact that charge-separation and charge-recombination are two different processes and cannot be treated the same way. It is, however, safe to assume that the trends observed for the charge-recombination in $C_{60}^{\bullet-}$-ZnP$^{\bullet+}$-Fc are in the inverted region, while that in $C_{60}^{\bullet-}$-ZnP-Fc$^{\bullet+}$ in the normal region. (Figure 8).

$$k_{ET} = \left[\left(\frac{4\pi^3}{h^2\lambda k_B}\right)^{1/2} V^2 \exp\left(-\frac{(\Delta G^{\circ}_{ET} + \lambda)^2}{4\lambda k_B T}\right)\right] \qquad (4)$$

Table 4. Rate constants for charge-recombination in 2c as a function of solvent polarity.

	k_{CR} / s^{-1}		
	chloro-benzene (ε_s = 5.62)	benzonitrile (ε_s =25.2)	dimethyl-formamide (ε_s = 36.7)
$C_{60}^{\bullet-}$–ZnP$^{\bullet+}$–Fc	3.12×10^{8}	1.00×10^{9}	1.20×10^{9}
$C_{60}^{\bullet-}$–ZnP–Fc$^{\bullet+}$	1.33×10^{8}	2.90×10^{5}	1.64×10^{5}

We next investigated the short- and long-range damping factors. For example, we used the charge-recombination $C_{60}^{\bullet-}$-ZnP$^{\bullet+}$-Fc and charge-shift kinetics of $C_{60}^{\bullet-}$-ZnP$^{\bullet+}$-Fc and C_{60}-ZnP$^{\bullet-}$-Fc$^{\bullet+}$ to yield the $C_{60}^{\bullet-}$-ZnP-Fc$^{\bullet+}$ charge-separated states. The corresponding values are 0.17 $Å^{-1}$ for the phenylene-acetylene bridge and 0.13 $Å^{-1}$ and 0.097 $Å^{-1}$ for the acetylene-phenylene bridges (Figures SP72-75). Both values are in sound agreement with previous findings on *p*-phenylene-acetylene bridges.[30-36] They also confirm that the flow of charges is nearly independent of the direction, i.e. phenylene-acetylene *vs*. acetylene-phenylene.

The corresponding damping factors for the long-distance charge recombination are 0.43 and 0.37 $Å^{-1}$ for the phenylene-acetylene/acetylene combination and phenylene-acetylene/acetylene-phenylene combination, respectively (Figures SP76-77). Considering that both values are appreciably smaller than that found in *meso*-linked multicomponent arrays[9] with 0.6 $Å^{-1}$, we conclude that *β*-linking assists in reducing the distance dependence at room temperature and, in turn, facilitates the overall flow of charges. Moreover, phenylene-acetylene-based bridges seem to be better conductors than purely acetylene based ones.

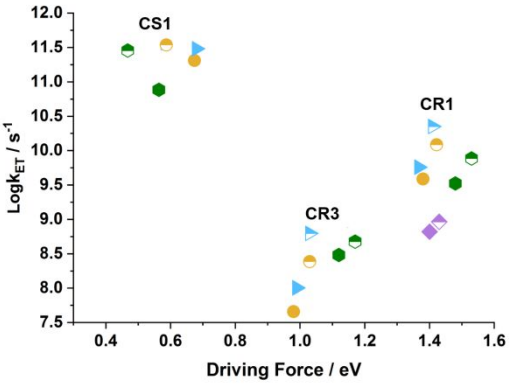

Figure 8. *Driving force (-ΔG°_{ET}) dependence of intramolecular charge-transfer rate constants in conjugates* ***1a*** *and* ***1b****. Purple half full diamonds, green half full hexagons, yellow half full circles, blue half full triangles represent the CS1, CR1, and CR3 in toluene, chlorobenzene, benzonitrile and dimethylformamide, respectively, for* ***1a****. Similarly, purple full diamonds, green full hexagons, yellow full circles, blue full triangles represent the CS1, CR1, and CR3 in toluene, chlorobenzene, benzonitrile and dimethylformamide, respectively for* ***1b****.*

To separate the charge-recombination dynamics, one of the obvious choices includes the combination of a low-damping-factor bridge to connect the C_{60}/ZnP couple and a high-damping-factor one to link the ZnP/Fc couple. We are currently working on the design and synthesis of such novel electron donor-acceptor conjugates.

Conclusions

Functionalization of a central ZnP in β-positions with two *p*-phenylene-acetylene bridges with C_{60} or Fc termini has been used to synthesize a series of C_{60}-ZnP-Fc electron donor-acceptor conjugates. By changing the reorganization energy, the damping factor, the electron donor-acceptor distance, and the solvent polarity, we gained full control over shuttling electrons and holes between C_{60}, ZnP, and Fc. Among the aforementioned, the damping factor of *p*-phenylene-acetylene bridges was the most important factor. On the one hand, two different charge-separation pathways, the $C_{60}^{\bullet-}$-$ZnP^{\bullet+}$-Fc *vs*. the C_{60}-$ZnP^{\bullet-}$-$Fc^{\bullet+}$ charge-separated state route, were activated in the initial deactivation of the ZnP singlet-excited state. On the other hand, two different charge-recombination pathways, Marcus inverted *vs* Marcus normal, evolved for the $C_{60}^{\bullet-}$-$ZnP^{\bullet+}$-Fc and $C_{60}^{\bullet-}$-ZnP-$Fc^{\bullet+}$ charge-separated states, respectively. All in all, a distant $C_{60}^{\bullet-}$-ZnP-$Fc^{\bullet+}$ charge-separated state is formed, which is longer-lived than the adjacent $C_{60}^{\bullet-}$-$ZnP^{\bullet+}$-Fc charge-separated state.

EXPERIMENTAL SECTION

General method.

^{1}H NMR spectra were measured on a Bruker AM-400 and Bruker 300 instruments. The chemical shifts were referenced to the residual peaks of the deuterated solvents: chloroform (7.26 ppm) and benzene (7.15 ppm).

ESI spectra were acquired used two different instruments. ESI-HRMS were performed with Orbitrap Q-Exactive (Thermo Scientific) in positive ion full scan mode by adopting the following parameters values: spray voltage between 5-6 kV depending on the compound, S-lens RF level = 100, sheat gas level = 50, auxiliary gas level = 10, capillary temperature = 320 °C, auxiliary gas heather = 300 °C, AGC target = 3x10e6, Max inj. Time = 120 ms, resolution power = 100000. Calculation of exact mass of each compound was performed by using Xcalibur software (Thermo Scientific) with an accuracy ≤ 5ppm. ESI-Q-TOF was performed with Synapt Q (Waters) in positive reflector mode. Acetonitrile was used as solvent. Capillary voltage was set to 3 kV, source temperature was 120°C and desolvation temperature was 150°C.

MALDI spectra were acquired using two different instruments. The first is a MALDI-TOF MS 4800 (AB Sciex) in positive reflector mode. The instrument is equipped with a Nd:YAG laser operating at 355 nm (200 Hz). 2,5-dihydroxybenzoic acid (2.5 mg/mL in CH_3CN/0.1% TFA) was used as matrix. Accelerating voltage was set to 20 kV and delay extraction to 400 ns. Each registered spectrum is the sum of 1500 laser shots. The second is a MALDI-TOF Reflex IV instrument (Bruker-Daltonics) in reflector mode, using a 337 nm nitrogen laser (8 Hz). A 2 mg/mL of a 2,5-dihydroxybenzoic acid (gentisic acid) solution in CH_3CN/TFA (0.1% solution) was used as matrix. It was used to detect the molecular weight of compound 3b. Its m/z Calcd refers to average molecular weight.

UV-visible absorption spectra were recorded on a Varian Cary 50 Scan spectrophotometer in CH_2Cl_2 and toluene solution.

UV/Vis spectra were collected at room temperature using a Perkin Elmer Lambda 2 spectrometer. The data were recorded with the software UV WinLab using a slit width of 2 nm and a scan rate of 480 nm/min.

Steady-state fluorescence studies were conducted using Fluoromax 3 spectrometer (Horiba Scientific).

To determine the quantum yields (QYs) the comparative method was used which involves the usage of well characterized standard references.

Electrochemistry data was collected by performing differential pulse voltammetry at room temperature. Application of potential was controlled with μAutolab III/FRA2 potentiostat from METROHM. To record the current vs. the applied potential voltammograms, NOVA 1.10 software was used. A home-made cell was used to perform the measurements in Ar-saturated dichloromethane with 0.1 M tetrabutylammonium hexafluorophosphate NBu_4PF_6 as the supporting electrolyte in a three-electrode configuration. Glassy carbon was used as working electrode (3 mm diameter), Pt wire acting as the counter electrode, and Ag wire as the quasi-reference electrode. The Fc/Fc^+ redox couple was used as an internal standard. The chemicals purchased from Acros Organics, Sigma Aldrich, and Alfa Aesar were used without any further treatment or purification.

Spectroelectrochemistry data was recorded with help absorption spectrometer Carry 5000 using a home -made three-electrode cell set up. The potential was applied to the cell using potentiostat from METROHM.

Time-resolved absorption studies were performed by using the Clark MXR CPA 2101 and CPA2110 Ti:sapphire amplifier

(775nm, 1 kHz, 150 fs pulse width) as the laser source. Ultrafast Systems HELIOS femtosecond transient absorption spectrometer was used to acquire time resolved transient absorption spectra with 150 fs resolution and time delays from 0 to 5500 ps. The probe-visible white light (~400−770 nm)-was generated by focusing a fraction of the fundamental 775 nm output onto a 2 mm sapphire disk. And, for the (near) IR (780−1500 nm), a 1 cm sapphire was used. Non-collinear optical parameter (NOPA, Clark MXR) was used to generate the excitation wavelength at 568 nm; a bandpass filter ± 10 nm was used to exclude the fundamental 775 nm and 387 nm. All measurements were conducted in 2 mm quartz cuvettes under argon atmosphere.

An Ultrafast Systems EOS sub-nanosecond transient absorption spectrometer was employed to measure transient absorption spectra with time delays of ~1 ns to 400 μs with 1 ns time resolution. White light (~370 to >1600 nm) was generated by a built-in photonic crystal fiber supercontinuum laser source with a fundamental of 1064 nm at 2kHz output frequency and pulse width of approximately 1 ns.

Multi-wavelength analyses were used to treat the obtained data from pump-probe experiments by using the Origin 2016 and 2018. Kinetic traces were fit using multi-exponential function. Additionally, the global-target analysis was performed using the open-source Glotaran software. The data points in the 765-790 nm regime was removed as they stem from the fundamental excitation wavelength.

X-ray Photoelectron Spectroscopy measurements were obtained from a modified Omicron NanoTechnology MXPS system. The spectra were excited by achromatic Mg Kα and Al Kα photons (hν = 1253.6 and 1486.6 eV, respectively), generated operating the anode at 14-15 kV, 10-20 mA. All the samples were mounted on metal tips as thin layers of pressed powders. Experimental spectra were theoretically reconstructed by fitting the peaks to symmetric pseudo-Voigt functions (linear combination of gaussian and lorentzian peaks) and the background to a Shirley or a linear function. XPS atomic ratios (±10% associated error) between relevant core lines were estimated from experimentally determined area ratios corrected for the corresponding theoretical cross sections and for a square root dependence of the photoelectron's kinetic energies. All binding energies were referenced to the lowest lying C 1s peak component, taken at 285.0 eV, which was assumed to be related to the aromatic C atoms.

Chemicals.

Silica gel 60 (70-230 mesh, Sigma Aldrich) was used for column chromatography. High-purity-grade nitrogen and argon gases were purchased from Rivoira. When anhydrous conditions were required the solvents were freshly distilled under nitrogen atmosphere and at ambient pressure, following the literature procedures. Toluene was distilled over sodium and THF over $LiAlH_4$. Fullerene-C60 was purchased from Term-USA. All the reagents and solvents were from Fluka Chem. Co., Aldrich Chem. Co. or Carlo Erba and were used as received.

H_2Br_2 compound was obtained as reported in literature; [43] **1**, **1H$_2$Br**, **CHO1H$_2$a**, **CHO1H$_2$b**, **1H$_2$a**, **1H$_2$b**, **1a** and **1b** compounds have been synthesized and reported in literature.[62] **b'**, **b**, **2**, **2H$_2$Br**, **CHO2H$_2$a**, **CHO2H$_2$b**, **2H$_2$a**, **2H$_2$b**, **2a** and **2b** compounds have been synthesized and reported in literature.[33] Compound **3** has been synthesized and reported in literature.[32]

Compound **c'**.

580 mg (2 mmol) of 4-(ferrocenyl)-phenylacetylene, 500 mg (1.67 mmol) of 1-iodo-4-(trimethylsilyl)ethynylbenzene and 165 mg (0.54 mmol) of $AsPh_3$ were dissolved in 230 mL of anhydrous toluene and 45 mL of anhydrous triethylamine under nitrogen atmosphere. The solution was deaerated using argon bubbling for 30 min., then 74 mg (0.07 mmol) of $Pd_2(dba)_3$ were added. The solution was deaerated for further 20 min., after that the argon inlet was placed 1 cm above the solution. The flow rate was increased slightly, and the reaction was left under nitrogen at 40°C for 16 h. The solvent was evaporated and the crude product was purified by column chromatography on silica gel eluting with petroleum ether (40°-70°)/diethyl ether (98:2). The fraction containing the desired product was collected and the solvent was removed under vacuum to give compound **c'** (160 mg, 0.35 mmol, 22%).

MALDI-TOF MS $C_{29}H_{26}FeSi$ $[M]^+$ *m/z* Calcd: 458.115 Found: 458.082; ^{1}H NMR (400 MHz, C_6D_6, 25 °C) δ = 7.50 (d, *J* = 8.0 Hz, 2H), 7.31 (m, 4H), 7.25 (d, *J* = 8.0 Hz, 2H), 4.43 (s, 2H), 4.11 (s, 2H), 3.68 (s, 5H), 0.25 (s, 9H) ppm.

Compound **c**.

500 mg (3.9 mmol) **c'** were dissolved in 20 mL of THF, then 5 mL of saturated solution of K_2CO_3 in CH_3OH were added. The mixture was left under nitrogen atmosphere and vigorous stirring for 3 h. The organic phase was washed with water (3x100 mL), dried over anhydrous Na_2SO_4 and filtered. The solvent was removed under vacuum to give compound **c** (1.5 g, 3.86 mmol, >99%).

MALDI-TOF MS $C_{26}H_{18}Fe$ $[M]^+$ *m/z* Calcd: 386.075 Found: 386.035; ^{1}H NMR (400 MHz, $CDCl_3$, 25°C) δ = 7.55 (s, 4H), 7.52 (s, 4H), 4.73 (s, 2H), 4.42 (s, 2H), 4.11 (s, 5H), 3.24 (s, 1H) ppm.

Compound **CHO2H$_2$c**.

50 mg (0.054 mmol) of **2H$_2$Br**, 42 mg (0.11 mmol) of **c** and 15 mg (0.047 mmol) of $AsPh_3$ were dissolved in 25 mL of anhydrous toluene and 5 mL of anhydrous triethylamine under nitrogen atmosphere. The solution was deaerated using argon bubbling for 30 min., then 6.5 mg (0.0063 mmol) of $Pd_2(dba)_3$ were added. The solution was deaerated for further 20 min., after that the argon inlet was placed 1 cm above the solution. The flow rate was increased slightly, and the reaction was left under nitrogen at 40°C for 16 h. The solvent was evaporated, and the crude product was purified by column chromatography on silica gel eluting with toluene. The fraction containing the desired product was collected and the solvent was removed under vacuum to give compound **CHO2H$_2$c** (35 mg, 0.03 mmol, 53%).s

HRMS $C_{87}H_{54}N_4FeO$ $[M]^+$ m/z Calcd: 1226.365 Found: 1226.364; ^{1}H NMR (400 MHz, C_6D_6, 25°C) δ = 9.55 (s, 1H), 9.41 (s, 2H), 8.91-8.65 (m, 5H), 8.16 (s, 4H), 8.05 (s, 5H), 7.62-7.32 (br m, 26H), 4.45 (s, 2H), 4.14 (s, 2H), 3.86 (s, 5H), -2.13 (s, 2H) ppm; UV-vis (CH_2Cl_2) λ_{max} (log ε) = 433 (5.43), 532 (4.4), 573 (4.25), 608 (3.99), 664 (3.73) nm.

Compound **2H$_2$c**.

35 mg (0.028 mmol) of **CHO2H$_2$c**, 30 mg (0.042 mmol) of C60 and 50 mg (0.56 mmol) N-methylglycine were refluxed for 72 h in 35 mL of anhydrous toluene under nitrogen atmosphere.

The solvent was removed, and the crude product was purified by column chromatography on silica gel eluting with toluene. Recrystallization from toluene/petroleum ether (40°-70°) gave compound **2H$_2$c** (10 mg, 0.005 mmol, 18%).

MALDI-TOF MS $C_{149}H_{59}FeN_5$ $[M+H]^+$ m/z Calcd: 1974.419. Found: 1974.347; ^{1}H NMR (400 MHz, C_6D_6, 25°C) δ = 9.40 (s, 2H), 8.89-8.69 (m, 4H), 8.23-8.14 (m, 5H), 8.13-8.05 (br m, 5H), 7.76-7.25 (br m, 26H), 4.89 (d, *J* = 5Hz, 1H), 4.49 (s, 1H), 4.44 (s, 2H), 4.38 (d, *J* = 9Hz, 1H), 4.13 (s, 2H), 3.87 (s, 5H), 3.24 (s, 3H), -2.18 (s, 2H) ppm; UV-vis (CH_2Cl_2) λ_{max} (log ε) = 434 (4.56), 532 (4.11), 573 (4.04), 609 (3.80), 667 (3.53) nm.

Compound **2c**.

32 mg (0.016 mmol) of **2H$_2$c** were dissolved in 35 mL of $CHCl_3$ and 2 mL of saturated solution of $Zn(AcO)_2$ in CH_3OH was added. Mixture was refluxed and stirred for 3 h. The solvent was removed under vacuum and the crude product was purified by a plug of silica gel eluting with chloroform. Recrystallized from CH_2Cl_2/CH_3OH gave compound **2c** (33 mg, 0.016 mmol, >99%).

ESI-Q-TOF MS $C_{149}H_{57}FeN_5Zn$ $[M]^+$ m/z Calcd: 2035.325 Found: 2035.548; ^{1}H NMR (400 MHz, C_6D_6, 25°C) δ = 9.55 (s, 2H), 9.02 (d, *J* = 1.8 Hz, 1H), 8.98 (s, 1H) 8.94-8.81 (m, 3H), 8.33-8.19 (m, 9H), 7.65-7.45 (br m, 14H), 7.38-7.28 (m, 6H), 7.06-6.94 (br m, 6H), 4.50 (s, 1H), 4.45 (s, 2H), 4.38 (d, *J* = 9.4 Hz, 1H), 4.12 (s, 2H), 3.88 (s, 5H), 3.67 (d, *J* = 8.5 Hz, 1H), 2.43 (s, 3H) ppm; UV-vis (Toluene) λ_{max} (log ε) = 444 (4.99), 568 (4.25), 608 (4.28) nm.

Compound **3H$_2$Br**.

194 mg (0.26 mmol) of **H$_2$Br$_2$**, 106 mg (0.32 mmol) of **3** and 115 mg (0.37 mmol) of $AsPh_3$ were dissolved in 50 mL of anhydrous toluene and 10 mL of anhydrous triethylamine under nitrogen atmosphere. The solution was deaerated using argon bubbling for 30 min., then 52 mg (0.05 mmol) of $Pd_2(dba)_3$ were added. The solution was deareated for further 20 min., after that the argon inlet was placed 1 cm above the solution. The flow rate was increased slightly and the reaction was left under nitrogen at 40°C for 16 h. The solvent was evaporated and the crude product was purified by column chromatography on silica gel eluting with toluene. The compound was recrystallized from CH_2Cl_2/CH_3OH to give compound **3H$_2$Br** (50 mg, 0.049 mmol, 19%).

HRMS for $C_{69}H_{41}N_4OBr$ $[M+H]^+$ m/z Calcd: 1021.254 Found: 1021.256; ^{1}H NMR (400 MHz, $CDCl_3$, 25°C) δ = 10.05 (s, 1H), 9.20-7.30 (br m, 38 H), -2.65 (s, 1H), -2.78 (s, 1H) ppm; UV-vis (CH_2Cl_2) λ_{max} (log ε) = 430 (5.15), 526 (4.25), 563 (3.88), 603 (3.75), 659 (3.63) nm.

Compound **CHO3H$_2$a**.

100 mg (0.098 mmol) of **3H$_2$Br**, 41 mg (0.20 mmol) of **a** and 30 mg (0.1 mmol) of $AsPh_3$ were dissolved in 50 mL of anhydrous toluene and 10 mL of anhydrous triethylamine under nitrogen. The solution was deaerated using argon bubbling for 30 min., then 14 mg (0.014 mmol) of $Pd_2(dba)_3$ were added to the solution. The mixture was deaerated again using argon bubbling for 20 min. The solution was left under nitrogen atmosphere and stirred at 40°C for 16 h. The solvent was removed under vacuum and the crude product was purified by column chromatography on silica gel eluting with toluene. Recrystallization from CH_2Cl_2/CH_3OH gave compound **CHO3H$_2$a** (56 mg, 0.048 mmol, 50%).

HRMS for $C_{81}H_{50}N_4OFe$ $[M+H]^+$ m/z Calcd: 1151.341 Found: 1151.345; ^{1}H NMR (400 MHz, C_6D_6, 25°C) δ = 9.53 (s, 1H), 9.46-9.35 (br m, 6H), 8.89-8.70 (br m, 8H), 8.18-8.07 (br m, 10H), 7.55-7.24 (br m, 23H), 4.40 (s, 2H), 4.16 (s, 5H), 4.05 (s, 2H), -2.09 (s, 2H) ppm; UV-vis (CH_2Cl_2) λ_{max} (log ε) = 432 (7.95), 523 (7.30), 580 (6.90), 611 (6.70), 670 (6.60) nm.

Compound **CHO3H$_2$b**.

47 mg (0.046 mmol) of **3H$_2$Br**, 26 mg (0.092 mmol) of **b** and 12 mg (0.04 mmol) of $AsPh_3$ were dissolved in 25 mL of anhydrous toluene and 5 mL of dried triethylamine under nitrogen atmosphere. The solution was deaerated using argon bubbling for 30 min., then 6 mg (0.0054 mmol) of $Pd_2(dba)_3$ were added. The solution was deareated for further 15 min., after that the argon inlet was placed 1 cm above the solution. The flow rate was turned up slightly and the reaction was stirred and under nitrogen at 40°C for 16 h. The solvent was removed under vacuum and the crude product was purified by column chromatography on silica gel eluting with toluene. Recrystallization from CH_2Cl_2/CH_3OH gave compound **CHO3H$_2$b** (30 mg, 0.024 mmol, 53%).

HRMS for $C_{87}H_{54}N_4OFe$ $[M]^+$ m/z Calcd: 1226.365 Found: 1226.369; ^{1}H NMR (400 MHz, C_6D_6, 25°C) δ = 10.06 (s, 1H), 9.10- 8.35 (m, 6H), 8.30-8.15 (m, 5H), 8.12-7.95 (m, 4H), 7.92-7.80 (m, 3H), 7.85-7.65 (m, 14H), 7.62-7.55 (m, 3H), 7.53-7.35 (m, 4H), 7.15-7.00 (m, 3H), 4.70 (d, *J* = 19.1 Hz, 2H), 4.40 (s, 2H), 4.10 (s, 5H), -2.60 (s, 1H), -2.65 (s, 1H) ppm; UV-vis (CH_2Cl_2) λ_{max} (log ε) = 432 (5.13), 528 (4.22), 572 (3.97), 606 (3.83), 665 (3.54) nm.

Compound **3H$_2$a**.

70 mg (0.061 mmol) of **CHO3H$_2$a**, 66 mg (0.091 mmol) of C60 and 108 mg (1.2 mmol) N-methylglycine were refluxed for 72 h in anhydrous toluene under nitrogen atmosphere. The solvent was removed and the crude product was purified by column chromatography on silica gel eluting with toluene. Recrystallization from toluene/petroleum ether (40°-70°) gave compound **3H$_2$a** (29 mg, 0.015 mmol, 25%).

MALDI-TOF MS $C_{143}H_{55}FeN_5$ $[M+H]^+$ m/z Calcd: 1898.388. Found: 1898.382; ^{1}H NMR (400 MHz, C_6D_6, 25°C) δ = 9.47-9.37 (br m, 6H), 8.90-8.67 (br m, 5H), 8.30-8.02 (br m, 9H), 7.65-7.26 (br m, 18 H), 4.89 (d, *J* = 4.6Hz, 1H), 4.41 (s, 3H), 4.32 (d, *J* = 4.6Hz, 1H), 4.14 (s, 5H), 4.05 (s, 2H), 3.23 (s, 3H), -2.13 (

s, 2H) ppm; UV-vis (Toluene) λ_{max} (log ε) = 336 (5.35), 433 (5.54), 526 (4.42), 577 (4.17), 610 (4.17), 668 (3.75) nm.

Compound **3H$_2$b**.

80 mg (0.065 mmol) of **CHO3H$_2$b**, 70 mg (0.098 mmol) of C60 and 115 mg (1.3 mmol) N-methylglycine were refluxed for 72 h in anhydrous toluene under nitrogen atmosphere. The solvent was removed, and the crude product was purified by column chromatography on silica gel eluting with toluene. Recrystallization from toluene/petroleum ether (40°-70°) gave compound **3H$_2$b** (35 mg, 0.018 mmol, 27%).

MALDI-TOF MS $C_{149}H_{59}FeN_5$ $[M+H]^+$ m/z Calcd: 1974.419. Found: 1974.612; ^{1}H NMR (400 MHz, C_6D_6, 25°C) δ = 9.47-9.40 (br m, 6H), 8.89-8.70 (br m, 10H), 8.28-8.03 (br m, 6H), 7.61-7.27 (br m, 20), 4.89 (d, *J* = 4.6 Hz, 1H), 4.54 (s,

2H), 4.41 (s, 1H), 4.32 (d, J = 4.6 Hz, 1H), 4.17 (s, 2H), 3.93 (s, 5H), 3.23 (s, 3H), -2.15 (s, 2H) ppm; UV-vis (Toluene) λ_{max} (log ε) = 333 (4.52), 431 (4.74), 525 (3.83), 572 (3.58), 607 (3.44), 664 (3.20) nm.

Compound **3a**.

29 mg (0.0153 mmol) of **3H$_2$a** were dissolved in 10 mL of $CHCl_3$ and 2 mL of saturated solution of $Zn(AcO)_2$ in CH_3OH were added. The mixture was refluxed for 3 h under nitrogen. The solvent was removed under vacuum and the crude product was purified by a plug of silica gel eluting with $CHCl_3$. Recrystallization from CH_2Cl_2/CH_3OH gave compound **3a** (30 mg, 0.0152 mmol, >99%).

MALDI-TOF MS $C_{143}H_{53}FeN_5Zn$ $[M]^+$ m/z Calcd: 1959.294. Found: 1959.156;^{1}H NMR (400 MHz, C_6D_6, 25°C) δ = 9.45-9.35 (br m, 6H), 8.93-8.65 (br m, 8H), 8.30-8.02 (br m, 9H), 7.65-7.26 (br m, 15 H), 4.52 (s, 1H), 4.46 (s, 2H), 4.39 (d, J = 9.2 Hz, 1H), 4.17 (s, 5H), 4.07 (s, 2H), 3.68 (d, J = 9.2 Hz, 1H), 3.0 (s, 3H) ppm; UV-vis (Toluene) λ_{max} (log ε) = 334 (4.80), 440 (4.97), 567 (3.92), 610 (3.93) nm.

Compound **3b**.

30 mg (0.0154 mmol) of **3H$_2$b** were dissolved in 10 mL of $CHCl_3$ and 2 mL of saturated solution of $Zn(AcO)_2$ in CH_3OH were added. The mixture was refluxed for 3 h under nitrogen. The solvent was removed under vacuum and the crude product was purified by a plug of silica gel eluting with chloroform. Recrystallization from CH_2Cl_2/CH_3OH gave compound **3b** (31 mg, 0.0152 mmol, >99% yield).

MALDI-TOF MS $C_{149}H_{57}FeN_5Zn$ $[M]^+$ m/z Calcd: 2038.33 Found:2037.68; ^{1}H NMR (400 MHz, C_6D_6, 25°C) δ = 9.61-9.53 (br m, 6H), 9.05-8.81 (br m, 8H), 8.42-8.08 (br m, 8H), 7.67-7.32 (br m, 20H), 4.74 (d, J = 4.7 Hz, 1H), 4.55 (s, 2H), 4.45 (s, 1H), 4.35 (d, J = 4.7 Hz, 1H), 4.17 (s, 2H), 3.94 (s, 5H), 3.16 (s, 3H) ppm; UV-vis (Toluene) λ_{max} (log ε) = 334 (5.06), 442 (5.45), 567 (4.34), 607 (4.36) nm.

Compound ***β*-ZnP-ref**.

30 mg of (0.032 mmol) of **2H$_2$Br**, 15 mg (0.064 mmol) of **2** and 11 mg (0.035 mmol) of $AsPh_3$ were dissolved in 20 mL of anhydrous toluene and 5 mL of anhydrous triethylamine under nitrogen atmosphere. The solution was deaerated using argon bubbling for 30 min., then 5.2 mg (0.005 mmol) of $Pd_2(dba)_3$ were added. The solution was deaerated for further 20 min., after that the argon inlet was placed 1 cm above the solution. The flow rate was increased slightly, and the reaction was left under nitrogen at 40°C for 16 h. The solvent was evaporated, and the crude product was purified by column chromatography on silica gel eluting with toluene. The fraction containing the desired product was collected and the solvent was removed under vacuum to give compound ***β*-ZnP-ref**. (20 mg, 0.02 mmol, 65%).

MALDI-TOF MS $C_{70}H_{40}N_4O_2Zn$ $[M]^+$ m/z Calcd: 1032.244 Found: 1032.192; ^{1}H NMR (400 MHz, $CDCl_3$, 25°C) δ = 10.10 (s, 2H), 9.30 (s, 1H), 9.27 (s, 1H), 9.05-8.7.68 (br m, 4H), 8.26 (br m, 5H), 7.98-7.64 (br m, 19H), 7.58 (br m, 5H), 7.44 (br m, 3H), ppm; UV-vis (CH_2Cl_2) λ_{max} (log ε) = 448 (5.43), 573 (4.4), 615 (4.4) nm.

ASSOCIATED CONTENT

Supporting Information

The Supporting Information is available free of charge on the ACS Publications website at DOI: xxxx.

Synthetic details and precursor's characterization, photophysical characterization, and theoretical calculations. (PDF)

AUTHOR INFORMATION

Corresponding Author

*Phone: +49 9131 8527341. Fax: +49 9131 85-28307. E-mail: dirk.guldi@fau.de.

*Phone: +39 06 7259 4759. Fax: +39 06 7259 4754. Email: pietro.tagliatesta@uniroma2.it

Author Contributions

The manuscript was written through contributions of all authors. ‡These authors contributed equally.

Funding Sources

This work was supported by the DeutscheForschungsgemeinschaft (DFG) via SFB 953 'Synthetic Carbon Allotropes'

Notes

The authors declare no competing financial interests.

ACKNOWLEDGEMENTS

RK, SB, and DMG thank the D DeutscheForschungsgemeinschaft (DFG) for funding the research through SFB 953 'Synthetic Carbon Allotropes. TC, and SB are thankful to the funding from Bavarian State Government as part of the Solar Technologies go Hybrid initiative.

ABBREVIATIONS

CS: charge-separation, CR: charge-recombination, CSh: charge-shift,

NBu_4PF_6: tetrabutylammoniumhexafluorophosphate

ZnP: Zinc porphyrin

Fc: Ferrocene

Pt: Platinum

REFERENCES

(1) Parson, W. W. Electron Donors and Acceptors in the in the Initial Steps of Photosynthesis in Purple Bacteria : A personal Account. *Photosynth. Res.* **2003**, *76*, 81–92.

(2) McConnell, I.; Li, G.; Brudvig, G. W. Review Energy Conversion in Natural and Artificial Photosynthesis. *Chem. Biol.* **2010**, *17*, 434–447.

(3) Wasielewski, M. R. Energy, Charge, and Spin Transport in Molecules and Self-Assembled Nanostructures Inspired by Photosyntheis. *J. Organomet. Chem.* **2006**, *71*, 5051–5066.

(4) Rudolf, M.; Kirner, S. V.; Guldi, D. M. A multicomponent molecular approach to artificial photosynthesis - the role of fullerenes and endohedral metallofullerenes. *Chem. Soc. Rev.* **2016**, *45*, 612–630.

(5) Imahori, H.; Yamada, H.; Guldi, D. M.; Endo, Y.; Shimomura, A.; Kundu, S.; Yamada, K.; Okada, T.; Sakata, Y.; Fukuzumi, S. Comparison of Reorganization Energies for Intra- and Intermolecular Electron Transfer. *Angew. Chem.* **2002**, *114*, 2450–2453.

(6) Schubert, C.; Margraf, J. T.; Clark, T.; Guldi, D. M. Molecualr Wires - Impact of π-conjugation ad implementation of molecular bottlenecks. *Chem. Soc. Rev*. **2015**, *44*, 988–998.

(7) Guldi, D. M.; Martín, N. Fullerene architectures made to order, biommetic motifs - design and features. *J. Mater. Chem.* **2002**, *12*, 1978–1992.

(8) Imahori, H.; Tkachenko, N. V.; Vehmanen, V.; Tamaki, K.; Lemmetyinen, H.; Sakata, Y.; Fukuzumi, S. An Extremely Small Reorganization Energy of Electron Transfer in Porphyrin-Fullerene Dyad. *J. Phys. Chem. A* **2001**, *105*,1750–1756.

(9) Imahori, H.; Tamaki, K.; Guldi, D. M.; Luo, C.; Fujitsuka, M.; Ito, O.; Sakata, Y.; Fukuzumi, S. Modulating Charge Separation and Charge Recombination Dynamics in Porphyrin- Fullerene Linked Dyads and Triads : Marcus-Normal versus Inverted Region. *J. Am. Chem. Soc.* **2001**, *123*, 2607–2617.

(10) Vail, S. A.; Krawczuk, P. J.; Guldi, D. M.; Palkar, A.; Echegoyen, L.; Tomé, J. P. C.; Fazio, M. A.; Schuster, D. I. Energy and Electron Transfer in Polyacetylene-Linked Zinc–Porphyrin–[60] Fullerene Molecular Wires. *Chem. Eur. J*. **2005**, *11*, 3375–3388.

(11) El-Khouly, M. E.; Han, K.-J.; Kay, K.-Y.; Fukuzumi, S. Stabilization of the Charge-Separated States of Covalently Linked Zinc Porphyrin–Triphenylamine–[60] Fullerene. *ChemPhysChem* **2010**, *11*, 1726–1734.

(12) Das, S. K.; Song, B.; Mahler, A.; Nesterov, V. N.; Wilson, A. K.; Ito, O.; D'Souza, F. Electron Transfer Studies of High Potential Zinc Porphyrin − Fullerene Supramolecular Dyads. *J. Phys. Chem. C* **2014**, *118*, 3994–4006.

(13) Sukegawa, J.; Schubert, C.; Zhu, X.; Tsuji, H.; Guldi, D. M.; Nakamura, E. Electron Transfer through Rigid Organic Molecular Wires Enhanced by Electronic and Electron–vibration Coupling. *Nat. Chem*. **2014**, *6*, 899–905.

(14) Guldi, D. M.; Fukuzumi, S. Electron Transfer in Electron Donor-Acceptor Ensembles Containing Porphyrins and Metalloporphyrins. *J. Porphyrins Phthalocyanines* **2002**, *6*, 289–295.

(15) Guldi, D. M.; Maggini, M.; Scorrano, G.; Prato, M. Intramolecular Electron Transfer in Fullerene/Ferrocene Based Donor-Bridge-Acceptor Dyads. *J. Am. Chem. Soc.* **1997**, *119*, 974–980.

(16) Wijesinghe, C. A.; El-Khouly, M. E.; Zandler, M. E.; Fukuzumi, S.; D'Souza, F. Charge-Stabilizing, Multimodular, Ferrocene–Bis(Triphenylamine)–Zinc- Porphyrin–Fullerene Polyad. *Chem. Eur. J.* **2013**, *19*, 9629–9638.

(17) Kirner, S. V.; Henkel, C.; Guldi, D. M.; Megiatto Jr, J. D.; Schuster, D. I. Multistep Energy and Electron Transfer Processes in Novel Rotaxane Donor – Acceptor Hybrids Generating Microsecond-Lived Charge Separated States. *Chem. Sci.* **2015**, *6*, 7293–7304.

(18) Albinsson, B.; P. Eng, M.; Pettersson, K.; Winters, M. U. Electron and Energy Transfer in Donor – Acceptor Systems with Conjugated Molecular Bridges. *Phys. Chem. Chem. Phys.* 2007, *9*, 5847–5864.

(19) Davis, W. B.; Ratner, M. A.; Wasielewski, M. R. Conformational Gating of Long Distance Electron Transfer through Wire-like Bridges in Donor - Bridge - Acceptor Molecules. *J. Am. Chem. Soc.* **2001**, *123*, 7877–7886.

(20) P. Eng, M.; Albinsson, B. Non-Exponential Distance Dependence of Bridge-Mediated Electronic Coupling. *Angew. Chem. Int. Ed.* **2006**, *45*, 5626–5629.

(21) Creager, S.; Yu, C. J.; Bamdad, C.; O' Connor, S.; MacLean, T.; Lam, E.; Chong, Y.; Olsen, G. T.; Luo, J.; Gozin, M.; Kayyem, J. F. Electron Transfer at Electrodes through Conjugated " Molecular Wire " Bridges. *J. Am. Chem. Soc.* **1999**, *121*, 1059–1064.

(22) Yzambart, G.; Zieleniewska, A.; Bauroth, S.; Clark, T.; Bryce, M. R.; Guldi, D. M. Charge-Gating Dibenzothiophene - S , S - Dioxide Bridges in Electron Donor − Bridge − Acceptor Conjugates. *J. Phys. Chem. C* **2017**, *121*, 13557–13569.

(23) Sikes, H. D.; Smalley, J. F.; Dudek, S. P.; Cook, A. R.; Newton, M. D.; Chidsey, C. E.; Feldberg, S. W. Rapid Electron Tunneling Through Oligophenylenevinylene Bridges. *Science* **2001**, *291*, 1519–1523.

(24) Figueira-Duarte, T. M.; Gégout, A.; Nierengarten, J.-F. Molecular and Supramolecular C_{60} − Oligophenylenevinylene Conjugates. *Chem.*

Commun. **2007**, *0*, 109–119.

(25) Torre, G. de la; Giacalone, F.; Segura, J. L.; Martín, N.; Guldi, D. M. Electronic Communication through P-Conjugated Wires in Covalently Linked Porphyrin/C_{60} Ensembles. *Chem. Eur. J.* **2005**, *11*, 1267–1280.

(26) Santos, J.; Illescas, B. M.; Wielopolski, M.; Silva, A. M. G.; Tomé, A. C.; Guldi, D. M.; Martín, N. Effecient Electron Transfer in β-substituted Porphyrin-C_{60} Dyads Connected Through a p-Pheynlenevinylene Dimers. *Tetrahedron* **2008**, *64*, 11404–11408.

(27) Helms, A.; Heiler, D.; McLendon, G. Electron Transfer in Bis-Porphyrin Donor-Acceptor Compounds with Polyphenylene Spacers Shows a Weak Distance Dependence. *J. Am. Chem. Soc.* **1992**, *114*, 6227–6238.

(28) Cohen, R.; Stokbro, K.; Martin, J. M. L.; Ratner, M. A. Charge Transport in Conjugated Aromatic Molecular Junctions: Molecular Conjugation and Molecule−Electrode Coupling. *J. Phys. Chem. C* **2007**, *111*, 14893–14902.

(29) Indelli, M. T.; Orlandi, M.; Chiorboli, C.; Ravaglia, M.; Scandola, F.; Lafolet, F.; Welter, S.; Cola, L. De. Electron Transfer Across Modular Oligo-p-Phenylene Bridges in Ru (Bpy)2 (Bpy-Phn-DQ)4 + (n = 1-5) Dyads. Unusual Effects of Bridge Elongation. *J. Phys. Chem. A* **2012**, *116*, 119–131.

(30) Atienza, C.; Insuasty, B.; Seoane, C.; Martín, N.; Ramey, J.; Rahman, G. M. A.; Guldi, D. M. Connecting Two C_{60} Stoppers to Molecular Wires: Ultrafast Intramolecular Deactivation Reactions. *J. Mater. Chem.* **2005**, *15*, 124–132.

(31) Wielopolski, M.; Atienza, C.; Clark, T.; Guldi, D. M.; Martín, N. p-Phenyleneethynylene Molecular Wires : Influence of Strucutre on Photoinduced Electron-Transfer Properties. *Chem. Eur. J.* **2008**, *14*, 6379–6390.

(32) Lembo, A.; Tagliatesta, P.; Guldi, D. M.; Wielopolski, M.; Nuccetelli, M. Porphyrin-Oligo-Ethynylenephenylene-[60]Fullerene Triads Synthesis and Electrochemical and Photophysical Characterization of the New Porphyrin-Oligo-PPE -[60]Fullerene Systems. *J. Phys. Chem. A* **2009**, *113*, 1779–1793.

(33) Limosani, F.; Possanza, F.; Ciotta, E.; Pepi, F.; Salvitti, C.; Tagliatesta, P.; Pizzoferrato, R. Synthesis and Characterization of Two New Triads with Ferrocene and C_{60} Connected by Triple Bonds to the Beta-positions of Meso-tetraphenylporphyrin *J. Porphyrins Phthalocyanines.* **2017**, *21*, 364-370.

(34) Possanza, F.; Limosani, F.; Tagliatesta, P.; Zanoni, R.; Scarselli, M.; Ciotta, E.; Pizzoferrato, R. Functionalization of Carbon Sphere with a Porphyrin-Ferrocene Dyad. *ChemPhysChem.* **2018**, *19*, 2243-2249.

(35) Göransson, E.; Boixel, J.; Fortage, J.; Jacquemin, D.; Becker, H.-C.; Blart, E.; Hammaström, L.; Odobel, F. Long-Range Electron Transfer in Zinc-Phthalocyanine- Oligo(Phenylene-Ethynylene)-Based Donor-Bridge-Acceptor Dyads. *Inorg. Chem.* **2012**, *51*, 11500–11512.

(36) Arero, J.; Kodis, G.; Schmitz, R. A.; Méndez-Hernández, D. D.; Moore, T. A.; Moore, A. L.; Gust, D. Design , Synthesis and Photophysical Studies of Phenylethynyl-Bridged Phthalocyanine-Fullerene Dyads. *J. Porphyrins Phthalocyanines* **2015**, *19*, 934–945.

(37) Kirk, M. L.; Shultz, D. A.; Stasiw, D. E.; Lewis, G. F.; Wang, G.; Brannen, C. L.; Sommer, R. D.; Boyle, P. D. Superexchange Contributions to Distance Dependence of Electron Transfer/Transport: Exchange and Electronic Coupling in Oligo(Para-Phenylene)- and Oligo(2,5-Thiophene)-Bridged Donor–Bridge–Acceptor Biradical Complexes. *J. Am. Chem. Soc.* **2013**, *135*, 17144–17154.

(38) Nakamura, T.; Fujitsuka, M.; Araki, Y.; Ito, O.; Ikemoto, J.; Takimiya, K.; Aso, Y.; Otsubo, T. Photoinduced Electron Transfer in Porphyrin-Oligothiophene-Fullerene Linked Triads by Excitation of a Porphyrin Moiety. *J. Phys. Chem. B* **2004**, *108*, 10700–10710.

(39) Tagliatesta, P.; Lembo, A.; Leoni, A. Synthesis and Characterization of Eight New Tetraphenylporphyrins Bearing One or Two Ferrocene on the β-pyrrole Positions. *New J. Chem.* **2013**, *37*, 3416-3419.

(40) Lembo, A.; Tagliatesta, P.; Guldi, D. M. Synthesis and Photophysical Investigation of New Porphyrin Derivatives with Pyrrole Ethynyl Linkage and Corresponding Dyad with [60] Fullerene. *J. Phys. Chem. A* **2006**, *110*, 11424–11434.

(41) Scarselli, M.; Limosani, F.; Passacantando, M.; D'Orazio, F.; Nardone, M.; Cacciotti, I.; Arduini, F.; Gautron E.; and Maurizio De Crescenzi, Influence of Iron Catalyst in the Carbon Spheres Synthesis for Energy and Electrochemical Applications, *Adv. Mater. Interfaces.* **2018**, *5*, 1800070 (1 of 10).

(42) Maggini, M.; Scorrano, G.; Prato, M. Addition of azides to fullerene C60: synthesis of azafulleroids *J. Am. Chem. Soc.* **1993**, *115*, 9798–9799.

(43) Di Carlo, G.; O. Biroli, A.; Pizzotti, M.; Tessore, F.;

Trifiletti, V.; Ruffo, R.; Abbotto, A.; Amat, A.; De Angelis, F.; Mussini, P. R. Tetraaryl ZnII porphyrinates substituted at β-pyrrolic positions as sensitizers in dye-sensitized solar cells: a comparison with meso-disubstituted push-pull Zn(II) porphyrinates. *Chem. Eur. J.* **2013**, *19*, 10723–10740.

(44) Through out the result section different references were used to compare the photophysical properties of the C_{60}-ZnP-Fc conjugates obtained from distinguished spectroscopic methods. For the absoprtion, and fluorescence spectroscopy, ZnTPP, and the ZnP-Fc conjugates: HZnPa, and HZnPb were employed as references. In case of electrochemistry, β-ZnP-ref., Fc-ref., and C_{60}-ref. were used to compare their redox potentials. The time-resolved absorption spectroscopy involves primarily comparison of the conjugates with β-ZnP-ref., and then with the HZnPa and HZnPb in order to confirm the involvement of the C_{60}-$ZnP^{\bullet-}$-$Fc^{\bullet+}$ charge-separated state.

(45) Binstead, R. A.; Crossley, M. J,; Hush, N, S. Modulation of Valence Orbtial Levels of Metallopoprhyrins by β-subsitution: Evidence from Spectroscopic and Electrochemical Studies of 2-Substituted Metallo-5, 10, 15, 20-tetraphenylpophyrins. *Inorg. Chem.* **1991**, 30, 1259-1264.

(46) Electrochemistry was performed in dichloromethane as it is one of the most common organic solvent used in combination with the supporting electrolyte NBu_4PF_6. Dichloromethane provides for the solubility and dissociation of the used supporting electrolyte which help to achieve good ionic conductivity. Moreover, it provides a wide potential window from −1.8 V to +1.75 V (Figure SP18).

(47) Rehm, D.; Weller, A. Kinetics of Fluorescence Quenching by Electron and Hydrogen-Atom Transfer. *Isr. J. Chem.* **1970**, *8*, 259–271.

(48) Verma, M.; Chaudhry, A. F.; Fahrni, C. Predicting the photoinduced electron transfer thermodynamics in Polyfluorinated 1,3,5- triarylpyrazolines Based on multiple linear free Energy Relationships. *Org Biomol Chem*. **2009**, *7*, 1536–1546.

(48) Yanai, T.; Tew, D. P.; Handy, N. C. A New hybrid Exchange-correlation Functional using the Coulomb-attenuating Method (CAM-B3LYP). *Chem. Phys. Lett.* **2004**, *393*, 51–57.

(49) Frisch, M. J.; Trucks, G. W.; Schlegel, H. B.; Scuseria, G. E.; Robb, M. A.; Cheeseman, J. R.; Scalmani, G.; Barone, V.; Petersson, G. A.; Nakatsuji, H.; Li, X.; Caricato, M.; Marenich, A. V.; Bloino, J.; Janesko, B. G.; Gomperts, R.; Mennucci, B.; Hratchian, H. P.; Ortiz, J. V.; Izmaylov, A. F.; Sonnenberg, J. L.; Williams-Young, D.; Ding, F.; Lipparini, F.; Egidi, F.; Goings, J.; Peng, B.; Petrone, A.; Henderson, T.; Ranasinghe, D.; Zakrzewski, V. G.; Gao, J.; Rega, N.; Zheng, G.; Liang, W.; Hada, M.; Ehara, M.; Toyota, K.; Fukuda, R.; Hasegawa, J.; Ishida, M.; Nakajima, T.; Honda, Y.; Kitao, O.; Nakai, H.; Vreven, T.; Throssell, K.; Montgomery, J. A. Jr.; Peralta, J. E.; Ogliaro, F.; Bearpark, M. J.; Heyd, J. J.; Brothers, E. N.; Kudin, K. N.; Staroverov, V. N.; Keith, T. A.; Kobayashi, R.; Normand, J.; Raghavachari, K.; Rendell, A. P.; Burant, J. C.; Iyengar, S. S.; Tomasi, J.; Cossi, M.; Millam, J. M.; Klene, M.; Adamo, C.; Cammi, R.; Ochterski, J. W.; Martin, R. L.; Morokuma, K.; Farkas, O.; Foresman, J. B.; Fox, D. J. Gaussian 16, Revision A.03, Gaussian, Inc., Wallingford CT, **2016**.

(50) Becke, A. D. Density-functional thermochemistry. III. The role of exact exchange. *J. Chem. Phys.* **1993**, *98*, 5648–5652.

(51) Peterson, K. A.; Woon, D. E.; Dunning, T. H. Jr. Benchmark calculations with correlated molecular wave functions. IV. The classical barrier height of the H+H2→H2+H reaction. *J. Chem. Phys.* **1994**, *100*, 7410–7415.

(52) Dunning, T. H. Jr. Gaussian basis sets for use in correlated molecular calculations. I. The atoms boron through neon and hydrogen. *J. Chem. Phys.* **1989**, *90*, 1007–1023.

(53) Caricato, M. Absorption and emission spectra of solvated molecules with the EOM-CCSD-PCM method. *J. Chem. Theory Comput.* **2012**, *8*, 4494–4502.

(54) Lipparini, F.; Scalmani, G.; Mennucci, B.; Cancès, E.; Caricato, M.; Frisch, M. J. A variational formulation of the polarizable continuum model. *J. Chem. Phys.* **2010**, *133*, 014106–014117.

(55) Scalmani, G.; Frisch, M. J. Continuous surface charge polarizable continuum models of solvation. I. General formalism. *J. Chem. Phys.* **2010**, *132*, 114110–114125.

(56) Cammi, R. Coupled-Cluster Theories for the Polarizable Continuum Model. II. Analytical Gradients for Excited States of Molecular Solutes by the Equation of Motion Coupled-Cluster Method *Int. J. Quantum Chem.* **2010**, *110*, 3040–3052.

(57) Miertuš, S.; Scrocco, E.; Tomasi, J. Electrostatic interaction of a solute with a continuum. A direct utilization of AB initio molecular potentials for the prevision of solvent effects. *Chem. Phys.* **1981**, *55*, 117–129.

(58) Miertuš, S.; Tomasi, J. Approximate evaluations of the electrostatic free energy and internal energy changes in solution processes. *Chem. Phys.* **1982**, *65*, 239–245.

(59) Pascual-ahuir, J. L.; Silla, E.; Tuñon, I. GEPOL: An Improved Description of Molecular Surfaces. 111. A New Algorithm for the Computation of a Solvent-Excluding Surface. *J. Comput. Chem.* **1994**, *15*, 1127–1138.

(60) Snellenburg, J. J.; Laptenok, S. P.; Seger, R.; Mullen, K. M.; van Stokkum, I. H. M. Glotaran: A Java-Based Graphical User Interface for the R Package TIMP. *J. Stat. Softw*. **2012**, *49*, 1–22.

(61) Another product which can result from the charge-recombination of C_{60}-$ZnP^{\bullet-}$-$Fc^{\bullet+}$ state is the triplet excited state of ferrocene, as it lies lower in energy (1.16 eV).[63] This is however impossible to probe due its extremely low extinction coefficient.

(62) Tagliatesta, P.; Pizzoferrato, R. Synthesis and characterization of new ferrocene, porphyrin and C_{60} triads, connected by triple bonds. *J. Organomet. Chem.* **2015**, *787*, 27-32.

(63) Araki, Y.; Yasumura, Y.; Ito, O. Photoinduced Electron Transfer Competitive with Energy Transfer of the Excited Triplet State of [60]Fullerene to Ferrocene Derivatives Revealed by Combination of Transient Absorption and Thermal Lens Measurements. *J. Phys. Chem. B* **2005**, *109*, 9843-9848.

Table of Contents artwork